VNiVERSiDAD D SALAMANCA

CAMPUS DE EXCELENCIA INTERNACIONAL

Ph.D. Thesis

Characterization of Topological-Protected Surface States in Three-dimensional Topological Crystalline Insulators

Author: Sanaz Mehdipour

Supervisor: Enrique Diez

A dissertation submitted
for the degree of Doctor of Philosophy
(Applied Physics)
in The University of Salamanca

2021

Contents

List of Figures

List of Tables

Abstract

Characterization of Topological-Protected Surface States in Three-dimensional Topological Crystalline Insulators

Sanaz Mehdipour

2021

In three-dimensional topological Insulators, the topological protected helical surface conducting states exist along with the bulk insulating states. In a class of topological insulators, namely topological crystalline insulators, the protection role of surface states is taken by crystalline symmetry instead of time-reversal symmetry. These exotic characteristics bring about potential applications in logic devices, thermoelectricity or quantum computers [**18**]. However, due to some critical challenges (like their compatibility with the existing devices, their fabrication processes as well as their compatibility with topological or quantum behavior under external stimuli, working temperature range, cost efficiency, practical structure and ease of use), topological materials are still lagging in device applications [**18**]. In this regard, this thesis aims at investigating the fundamental properties of a topological crystalline insulator, $Pb_{0.77}Sn_{0.23}Se$, based on Raman characterization at different temperature ranges and low magnetic fields as well as magneto-transport of its Hall bar devices at low temperatures, albeit with meeting challenges in fabrication and characterization. The Raman response of this material at relaxed conditions confirms the presence of topological surface states. Moreover, temperature-dependent Raman characterizations indicate that both surface states and their bulk counterparts contribute to the Raman response considering the interplay of electrons and phonons. Furthermore, our findings based on magnetic-field dependent Raman characterization demonstrate that the surface states are topologically protected by symmetry. These Raman results are also corroborated with magneto-transport characterizations, revealing the prominent role of an inherent attribute of this material based on strong spin-orbit coupling. Our results pave the way for electron studies in field-effect transistors based on topological phase transitions.

Acknowledgements

First and foremost I would like to thank my advisor, Enrique Diez for giving me an opportunity to pursue my PhD studies under his supervision within the past four years. Next, I would like to thank Geetha Balakrishnan at university of Warwick for providing me with the $Pb_{0.77}Sn_{0.23}Se$ material to learn about topological insulators experimentally. I also would like to thank Vittorio Bellani at university of Pavia for guiding me through Raman studies with his so much patience and great enthusiasm for science. I am deeply indebted to him for his always support and encouragement during my studies. Undoubtedly, I forever cherish the memory of learning from Vittorio. I also would like to thank Luis Plaja, the coordinator of experimental Physics department, who has devoted much of his precious time to facilitate the fields for students, besides his academic activities. Lastly, I would like to thank Mercede Velazquez and Mario Amado for giving me permission to work with Raman and Teslatron equipment in Raman spectroscopy and low temperature laboratories, respectively. As a whole I would like to thank all present and past members of nanotechnology group.

I would like to thank Alberto Rodriguez, a very approachable and modest guy whom I had the pleasure to assist in Mechanics (Physics) laboratory for a semester. His meticulous attention to details and respectful attitudes towards students is highly commendable. Jose Antonia Novoa gave me training in optical lithography in a pretty impressive and fun way inspired by “Star Wars” movies, so I would like to thank him in the same way: “Thanks Mr. Yoda ☺ May the force be with you!” I also would like to thank David Lopez and Yoann Lechaux, two dynamic and upbeat guys whom I learnt a lot from. Finally, I would like to thank Stephan Roche, one of my top 10 role models in both science and humanity. Whenever I had questions that I weren’t sure who to ask, the very first references that I looked up were Stephan’s books. His lectures and talks are always my favorite ones and sources of inspiration where I find my knowledge like a tiny drop of water with respect to his ocean of knowledge.

Last but not least, I would like to thank “*Junta de Castilla y Leon*” where I have received a prestigious scholarship for my PhD studies.

Introduction

The development and invention of tools to observe, manipulate and have control over the nanoparticles have revolutionized nanotechonology, which based on media coverage seems a new field, however in reality it goes back at centuries ago where our ancestors made gold nanoparticles but at that time they did not have microscope to observe them [3]. Nowadays, nanofabrication consists of four main parts: lithography, thin films, pattern transfer and metrology [3]. Lithography is the science of printing fine traces on the wafer. Thin film is the process of depositing metal or dielectric films. Pattern transfer is the process of transferring the printed image from lithography to the substrate or thin film. In order to accurately characterize the too tiny fabricated components, some tools like electron microscopy and atomic force microscopy are required rather than optical microscope, known as metrology [3].

To investigate the crucial roles of electrons and phonons in fabricated devices in studying their electronic properties and vibrational response of system structure to photons, some device characterizations using different techniques like Raman spectroscopy and transport measurements should be performed at special conditions to have more control on the measurements and probe the fundamental properties of the material under study. In this regard, this thesis focuses on fabrication and characterization of Hall bar devices of a topological crystalline insulator, $Pb_{0.77}Sn_{0.23}Se$. It starts with concise but complete describing the fabrication and characterization tools and techniques in chapter 1. Thereafter, chapter 2 elaborates on the essential topological terms and then the rest of chapter 2 is devoted to the Characterization results and interpretation. Finally, the dissertation ends in Chapter 3 with concluding remarks and a potential outlook.

Chapter 1 Inside the Cleanroom and Low Temperature Laboratory

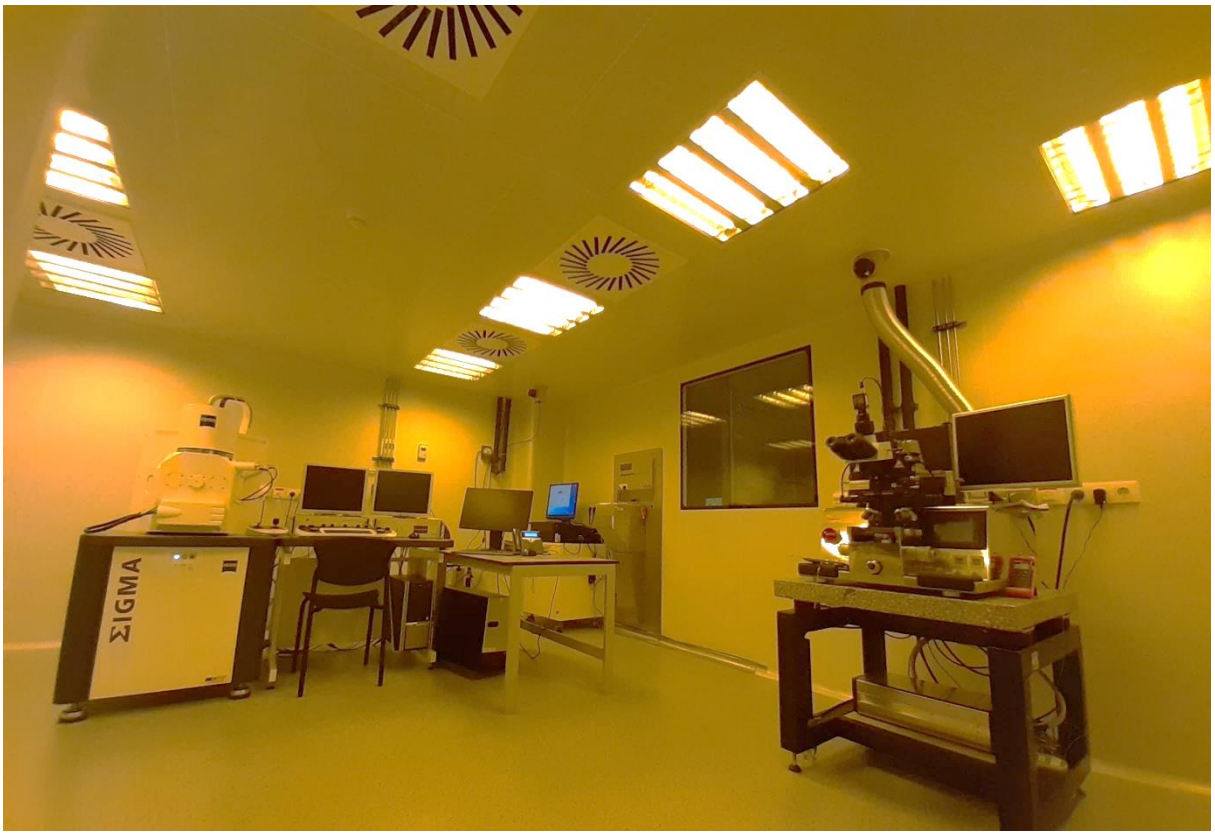

"I am among those who think that science has great beauty. A scientist in his laboratory is not only a technician: he is also a child placed before natural phenomena which impress him like a fairy tale".

- *Marie Curie*

This chapter may lay the foundation for the importance of understanding the fabrication and characterization techniques, tools and their limitations upon which the rest of this thesis, dealing with fabrication and characterization of Hall-bar devices is built. The science and technology of device fabrication involves a large number of techniques drawing from material science, electromagnetics, electronics and chemistry in a multidisciplinary manner [3]. Vacuum and plasma are two integral parts of every cleanroom, since vacuum is required for achieving high-purity conditions during a process as well as reducing molecular scattering. Moreover, in most semiconductor processes, a vacuum system is necessary before creating plasma [3]. Therefore, this chapter starts with a brief definition of cleanroom, vacuum and plasma. Thereafter, lithography, thin film and metrology are described. Lithography is a technique used for creating structures in the lateral direction, while thin-film deposition is used for creating precise structures in the vertical direction.

1.1 Introduction to the cleanroom concept

In today's society, different industries depending on their applications (See **Figure 1**) need some clean and containment environment for manufacturing. Indeed, the cleanroom concept is borrowed from the control of infection in hospitals that goes back at least 100 years during the era of Pasteur, Koch, Lister and other pioneer and microbiologists and surgeons [1].

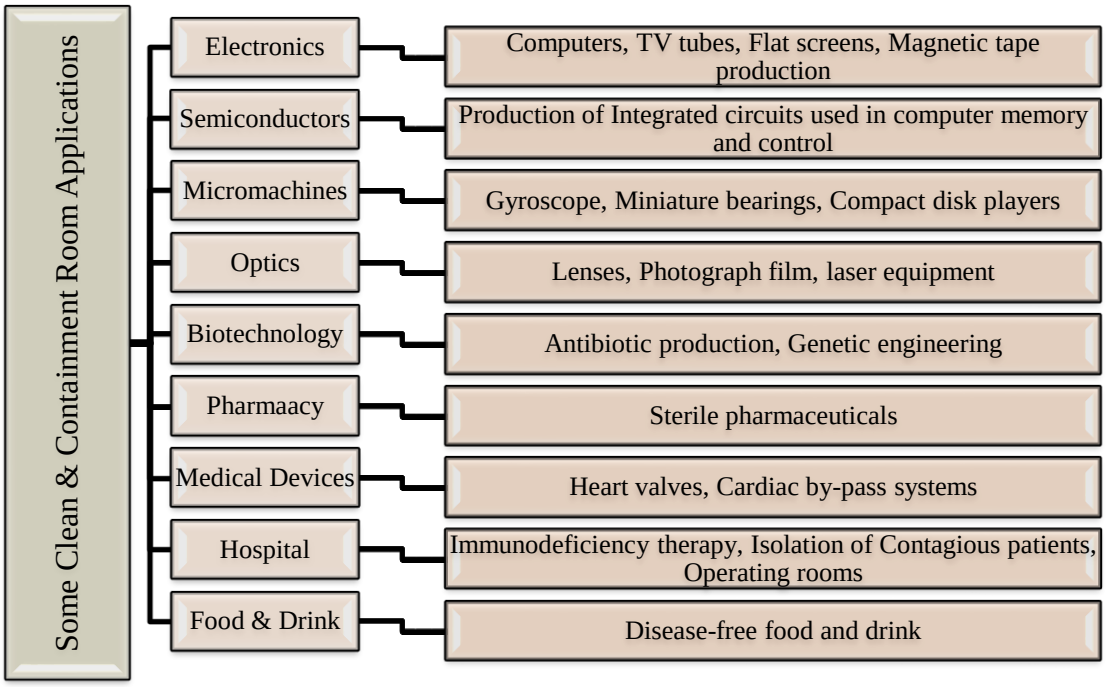

Figure 1: Some clean and containment room applications [1].

The challenging aspect of the evolution of yesterday's cleanroom into the modern one has been the ventilation by filtered air [1]. In parallel, in the engineering industries, the production of high efficiency particulate air (HEPA) filters with an integral fan known as fan filter units (FFUs) was the resultant of drastic measures to lower the levels of airborne contamination in the cleanrooms which were the copies of operating rooms in design and practice [1].

The first federal standard 209 produced by Sandia team is considered as the basis of most world cleanroom standards [1]. The definition of cleanroom in **Federal Standard 209 E** is: "*A room in which the concentration of airborne particles is controlled and which contains one or more clean zones*" [1].

And in **ISO 14644-1**:

"*A room in which the concentration of airborne particles is controlled, and which is constructed and used in a manner to minimize the introduction, generation, and retention of particles inside the room and in which other relevant parameters, e.g. temperature, humidity and pressure are controlled as necessary*" [1].

The classification of cleanrooms is done according to how clean their air is in terms of the size distribution of particles within a fixed volume of air at atmospheric pressure. **Table I** shows the ISO classification based on the following equation [1, 2]:

$$C_n = 10^N \times [\frac{0.1}{D}]^{2.08} \quad (1.1)$$

where

- C_n: the maximum permitted concentration of airborne particles (in particles/m^3 of air),
- N: the ISO classification number,
- D: the considered particle size in µm,
- 0.1: a constant with a dimension of µm.

The difference between the **Federal standard 209** and the **ISO 14644-1** are indeed in their dimension. The former is expressed in $\text{particles}/\text{ft}^3$, while the latter is expressed in $\text{concentration}/\text{m}^3$ [1].

In general, there are four types of clean areas, namely conventional, unidirectional flow, mixed flow as well as isolators and microenvironment [1]. The working principle of a conventional turbulently ventilated system formulates an idea of removing contamination by mixing and dilution. The quality and quantity of the air supplied to the room as well as the efficiency of mixing of the air determine the airborne cleanliness of the room [1]. Therefore, some parameters differentiate the ventilation in cleanrooms from an ordinary ventilated room [1]:

1. increased air supply,
2. high efficiency filters,
3. terminal air filters,
4. room pressurization, and
5. pass-through grills.

Figure 2 depicts a conventionally ventilated clean room [1], being considered as ISO 6 (class 1000) during manufacturing [1]. For instance, the cleanroom of university of Salamanca has three sections: dressing room, evaporation room and lithography room

that the first two sections are considered as ISO 7 and the last belongs to ISO 6 classification, respectively, see **Figure 3**. It is common to find containment cabinets with the same design technology of cleanroom itself inside a cleanroom, see **Figure 4**. The idea behind the design of pass-through grills (or dampers) at a low level on walls or doors is to create positively pressurized clean room with respect to the dirtier areas to have an air movement from the cleanest to the less clean rooms, see **Figure 2** [1].

On the other hand, other determining factors in cleanliness are the number of people working in the cleanroom, their activities and the quality of their garments. Therefore, it is necessary that the people working in the cleanroom wear well-designed clothing (coverall, knee length boots, hoods, gloves, etc.) to reduce particle generation due to their fallen hair, dead skin, the oil and dirt of their hands, their clothes threads, etc [1].

Table I: Cleanroom classifications based on particle counts [1].

Class	Particles≥0.5µm/ft^3 (maximum)	ISO Classification Number (N)
1	1	Class 3
10	10	Class 4
100	100	Class 5
1000	1000	Class 6
10000	10000	Class 7
100000	100000	Class 8

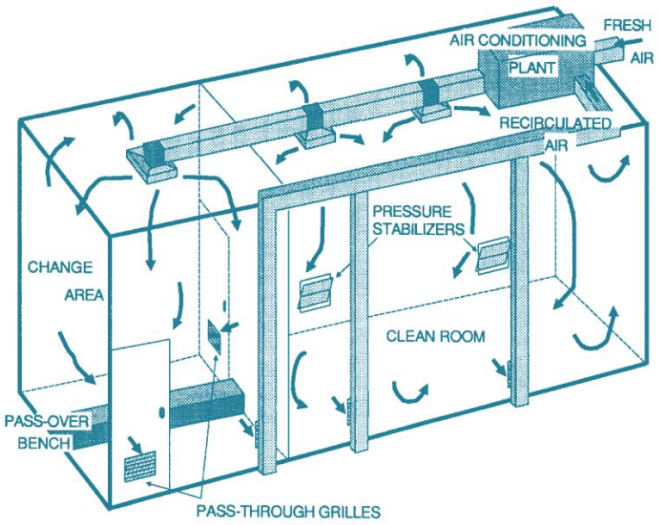

Figure 2: Conventionally ventilated cleanroom, figure is from [1].

Figure 3: The lithography room and dressing room of the University of Salamanca cleanroom, belonging to ISO 6 and ISO 7, respectively.

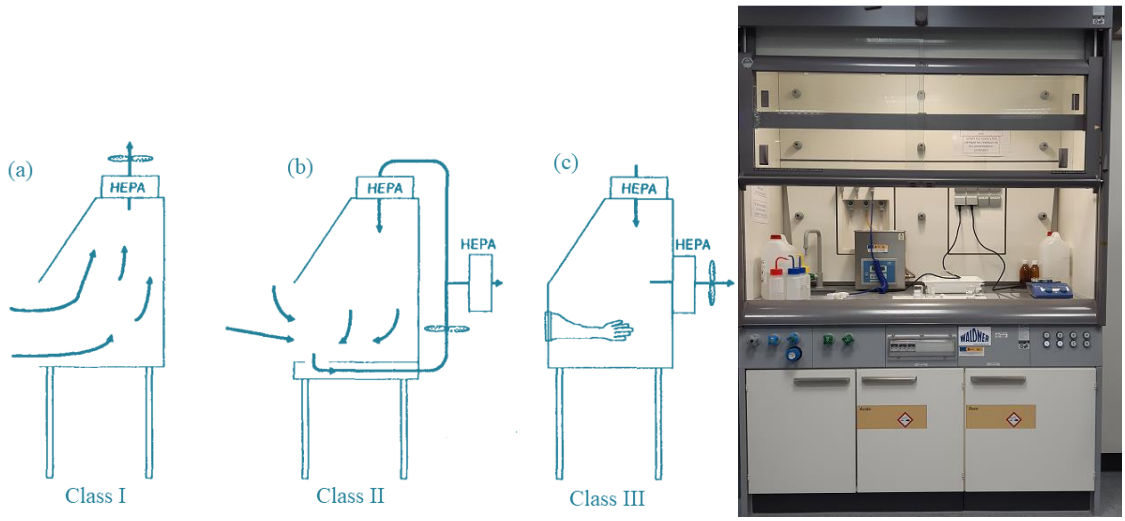

Figure 4: Left: Three classes of containment cabinets according to their airflow and application, figure is from [1]; **Right:** The containment cabinet class I in the evaporation room of the university of Salamanca cleanroom.

1.2 The Pressure Ranges in Vacuum technology and their characterization

A vacuum is a space from which air or other gases has been removed. Among the major constituents of air are N_2 (78.08 %), O_2 (20.94 %) and CO_2 (0.03 %). However, depending on the atmospheric condition, the contribution of water vapor (H_2O), as the

third largest constituent of air, becomes prominent [2, 3]. The type of the application decides how much air or any other gases should be removed (the vacuum level) [3]. There are four main regimes in division of the pressure range in vacuum technology, see **Figure 5** [4].

In vacuum technology, there are three types of flow [4]:

1. **Viscous (continuous) flow:** The viscous (continuous) flow is the typical flow in the rough vacuum range due to the intersection of the molecules. In this regime, the molecules' mean free path is considerably shorter than the diameter of the pipe [4].
2. **Molecular flow:** The molecular flow is expected in high and ultrahigh vacuum ranges. Indeed, in this regime the mean free path length for a particle is very much larger than the diameter of the pipe [4].
3. At the transition between these two the so-called Knudsen flow, which occurs in the medium vacuum range [4].

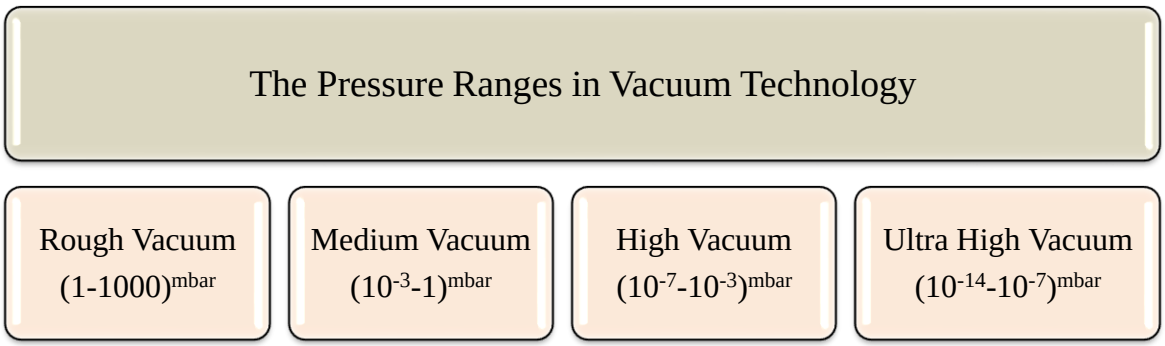

Figure 5: The pressure range regimes in vacuum technology [4].

The gas flow through any desired piping element (pipes or hoses, valves, nozzles, …) is indicated with $Q = C\Delta P$, which is equivalent to "ohm's law" for vacuum technology; where ΔP is the pressure difference across the component, C (volume/time (l/s)) is the conductance, affected by the geometry of the piping element. The conductance strongly depends on the flow type regime and thus pressure. In the high and ultrahigh vacuum ranges (molecular flow), C is constant and independent of pressure;

while in the rough (viscous flow) and medium vacuum range (Knudsen flow), C is pressure dependent [4].

Generally, the pump system is connected to a vacuum system through the valves, separators, cold traps and so on. Therefore, the effective pumping speed (S_{eff}) is always less than the pumping speed (S) of the pump alone, as the flow undergoes the impedance by the connections between pump and vacuum system [4]. Thus, we have:

$$\frac{1}{S_{eff}} = \frac{1}{S} + \frac{1}{C_T} \tag{1.2}$$

where C_T is the total conductance value for the connection system made up of the individual values for different components connected in series (valves, baffles, separators, etc.) equal with [4]

$$\frac{1}{C_T} = \frac{1}{C_1} + \frac{1}{C_2} + \cdots + \frac{1}{C_n} \tag{1.3}$$

1.2.1 Vacuum Pumps

Vacuum pumps are being used to reduce the gas pressure in a certain volume and thus the gas density. Any vacuum system either simple or complicated is a combination of pumps, valves and pipes. Generally, vacuum pumps due to their working principle belong to two main classes [4]:

1. **Gas transfer vacuum pump:** the gas particles are removed from the volume into the atmosphere through one or several compression stages by means of displacement or pulse transfer [4].
2. **Entrapment vacuum pump:** the gas particles are removed by being trapped on a solid surface either by condensation or by chemical bonding (on the volume boundary) [4].

Figure 6 depicts the classification of vacuum pumps [4]. Two determining factors in choosing the proper pumps are pumping speed (expected to be high) and

backstreaming[1] (expected to be low), with the ability to provide a vacuum, free of particulate contamination [2]. Two versatile pumps in a cleanroom are turbomolecular (molecular regime) and scroll (viscous regime) pumps.

- **Turbomolecular pumps**

Turbo molecular pump belongs to the class of high vacuum pumps, practically providing a vacuum with ultimate pressure of $10^{-6}\ mbar$. As its exhaust pressure is in the molecular or transition regime, it should be accompanied by a backing pump (a rotary vane, screw, scroll or diaphragm pump). The very clean high vacuum provided by turbomolecular pump can be explained by its compression ratio directly associated with the mass of the molecules. Therefore, they can pump heavy hydrocarbon molecules so well, while at very low pressures due to their considerably lower compression ratio, the residual gas is composed mainly of light gases like H_2 originating from the metal walls of the chamber. Consequently, the ultimate pressure of a turbomolecular pump is dicided by the compression ratio for light gases [2, 4]. **Figure 7** depicts a turbo molecular pump.

- **Scroll pump:**

The scroll pump is a relatively simple compressor consisting of two surfaces, one fixed and one orbiting. The ultimate pressure achieved by this pump is $10^{-3}\ mbar$. Their small size, and oil-free feature as well as low cost of repair and maintenance make them the first choice as a backing pump to turbomolecular pumps in comparison with their peer oiled rotary pumps [2, 4]. **Figure 8** depicts a scroll pump.

[1] Reverse flow of any gas, vapor, or material from the pump [2].

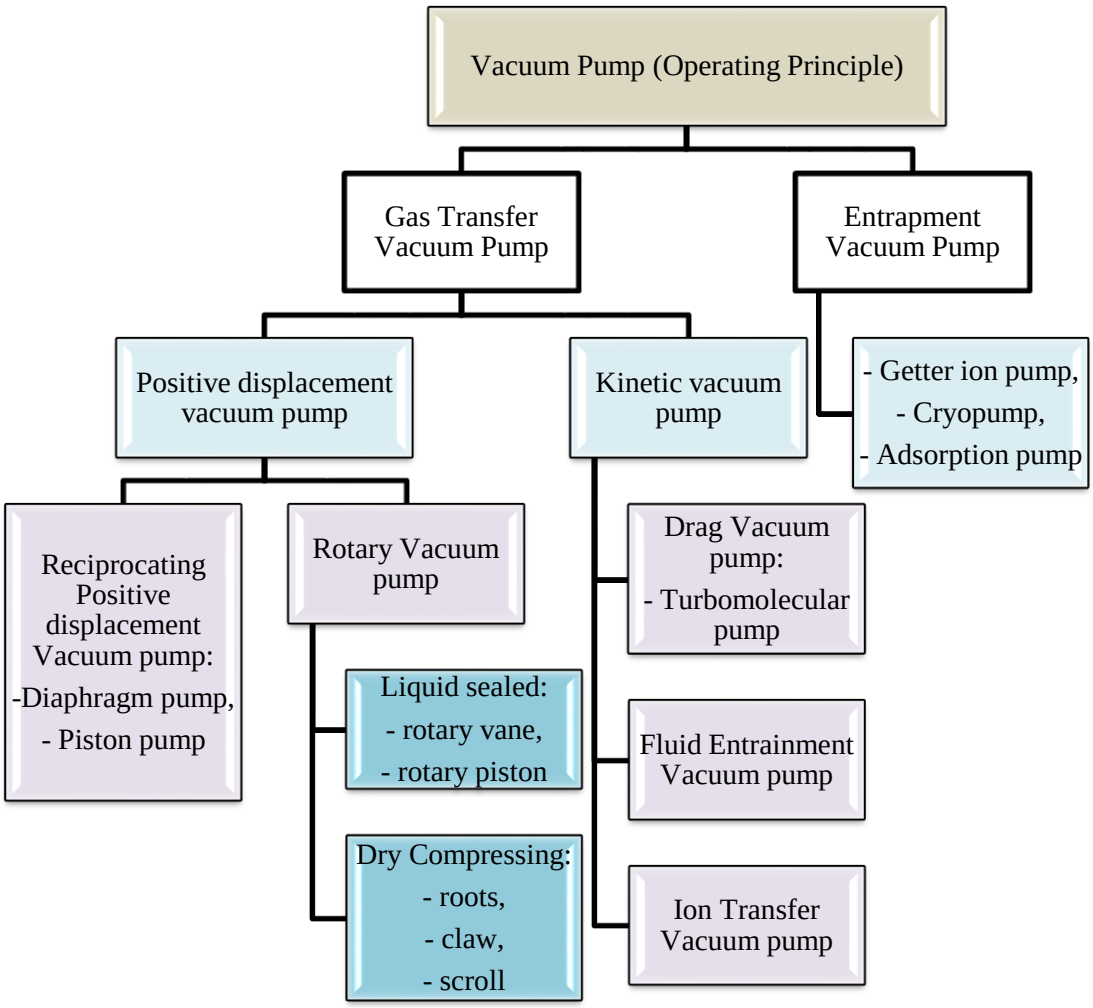

Figure 6: The classification of vacuum pumps [4].

Figure 7: A vertical turbomolecular pump connected to the load-lock of the e-beam evaporator.

Figure 8: A scroll pump is used as a backing pump of a turbomolecular pump for the scanning electron microscope equipment.

1.3 Plasma

Plasma is known as the fourth state of matter together with solid, liquid and gas, described as a quasi-neutral gas of charged and neutral particles with a balance between the densities of electrons and positive ions [5]. The plasma is generally divided into two main groups according to its ionization degree (the ratio of charged species density to that of neutral gas):

1. completely ionized plasma (the ionization degree is close to unity) and
2. weakly ionized plasma (the ionization degree is low) [5].

Generally, in laboratories, Plasma is generated by electrical discharges. Glow discharge and radio frequency (RF) are two plasma sources vastly being employed in modern microelectronic cleanrooms [3, 5]. The very common configuration of the electrical discharge Plasma is two parallel plates separated by a distance in a chamber, connected to a power supply. The gap between the two plates is evacuated and then filled with the desired Plasma gas. Therefore, in order to provide a constant pressure and a constant density of Plasma species in the chamber as well as preventing the accumulation of contaminants and byproducts in the chamber, the pump and the gas flow are kept continuously running [3, 5].

As depicted in **Figure 9**, in glow discharge type of Plasma as a weakly ionized non-equilibrium low-pressure non-thermal Plasma, there is a sequence of dark and bright luminous layers in a Plasma tube between cathode and anode. The electron mean free path and pressure decide a typical size of the layers [3, 5]. The observed glow is the resultant of ion-electron recombination and emitted photons. Therefore, depending on the gas species present in the Plasma and its photon energies, it is expected to observe a specific color. For instance, Argon emits a deep purple color, neon emits the well-known bright orange color, and oxygen emits a bluish-white color [3, 5].

The other non-thermal and non-equilibrium type of Plasma, widely employed in electronics and high-precision surface treatment technologies is low-pressure RF plasma. The upper and lower bounds of RF frequencies are determined by the wavelengths close to the system sizes, ionization and ion transfer frequencies. Non-thermal RF discharges can be either capacitively (CCP) or inductively (ICP) coupled [5].

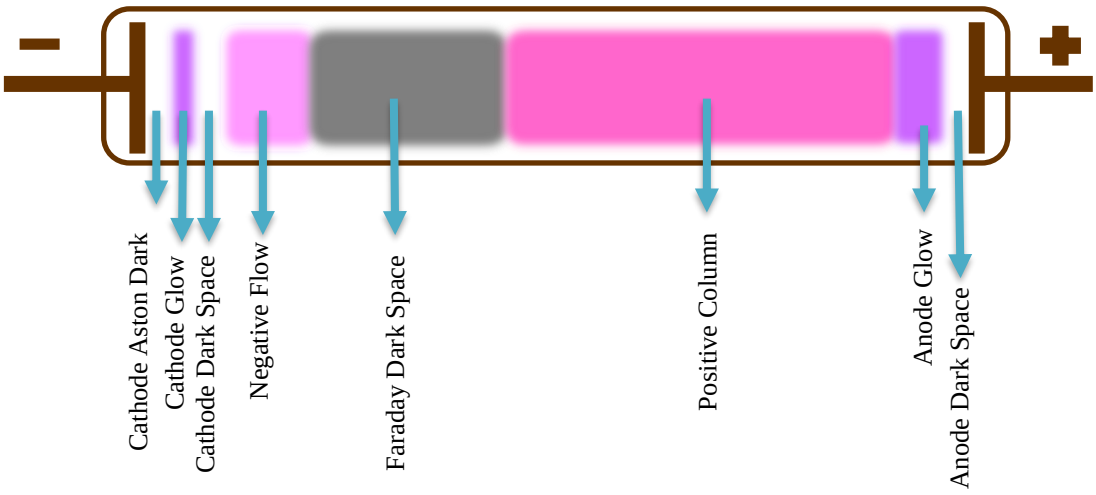

Figure 9: A sequence of dark and bright luminous layers in a Plasma tube.

1.4 Plasma Etching

Wet chemical and plasma etching (dry etching) are two common methods being employed in research laboratories to remove portions of a thin film (or substrate) by chemical or physical processes. The general configuration of a Plasma etching system is a vacuum chamber with a controlled gas in-flow rate and a throttled pumping rate to

control the chamber pressure. The cathode electrode is energized by an RF source and the substrate to be etched is placed on this electrode, see **Figure 10** (a) [3]. Etching can be done at room temperature or even below room temperatures. Due to the exponential dependence of etch rates on temperature, the wafer temperature needs to be maintained constant and uniform to achieve a consistent and reproducible etch rate, albeit with unexpected effects of Plasma heating and etch reaction itself [3]. The widely used approach in etch reactors to maintain a constant temperature is known as back-side helium cooling to provide good thermal contact to the wafer without any heat transfer compounds or pastes [3]. The ICP configuration is widely used in Plasma etching. Applying another RF source to the wafer electrode results in a negative DC bias on the electrode, known as the bias power or RIE power, without affecting the Plasma density or the ion density. This configuration is known as an ICP-RIE system [3].

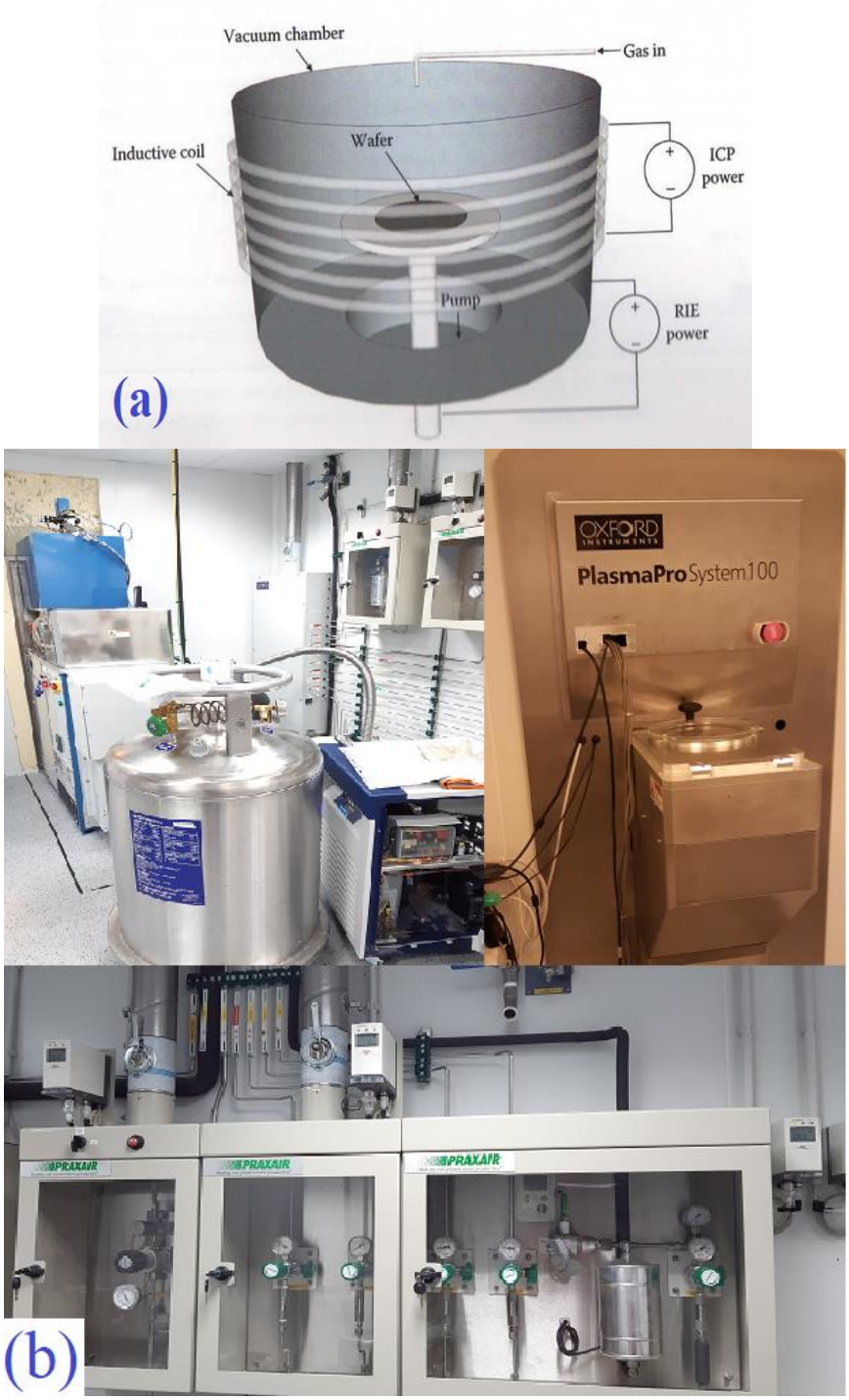

Figure 10: (a) Schematic of ICP-RIE plasma configuration, figure is from [3], **(b)** the ICP-RIE set-up in the clean room of university of Salamanca.

1.5 Optical Lithography

Fabrication of different types of electrodes over substrates requires some physical and chemical processes to be performed. The main process is patterning which is strongly dependent on lithography [6]. Optical lithography is a subject of lithography that uses photons to define the lateral structures. In an optical lithography process, a light-sensitive polymer, called a photoresist, is exposed and developed to form 2D relief images on the substrate. The general sequence of processing steps for a typical optical lithography process is [6]:

1) Substrate preparation;
2) Photoresist spin coating;
3) Post-apply baking;
4) Exposure;
5) Post-exposure baking;
6) Development; and
7) Post baking.

Photoresists has three main components: solvent, resin and photoactive compound (PAC), see **Figure 11** [3].

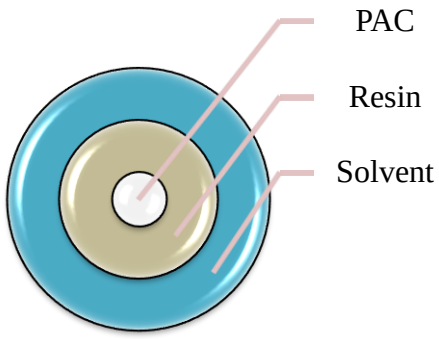

Figure 11: Components of a photoresist [3].

During the spin coating, the key role of dispensing liquid and viscosity modification is taken by solvent. By post-apply baking which is done after spin coating, the solvent is removed [3]. Therefore, the resin takes the main role as the “resist” part of

the photoresist; while the PAC takes the “photo” role as it is the UV-sensitive component of the photoresist [3]. Generally, the photoresists are divided into two main groups based on the solubility of the resist in a developer upon exposure to light: positive-tone photoresists and negative-tone photoresists. In case of positive-tone photoresists, the solubility of the photoresist increases after exposure, whereas the opposite is true in case of negative-tone photoresists [3].

- **Substrate Preparation**

In order to improve the adhesion of the photoresist material to the substrate and to have a contaminant-free resist film, it is necessary to take the following approaches:

1. Substrate cleaning to remove contamination, and
2. Dehydration bake to remove water [3]

Among variety of approaches to clean the silicon wafers in the research laboratories, the acetone-methanol-isopropyl alcohol (AMI) cleaning is the simplest and most widely used process to remove organic contaminations from the substrate (including photoresist) [3]. Cleaning the substrate in acetone, results in dissolving a large number of organic residues, which leaves an organic film behind. For this reason, methanol is used to dissolve acetone before it dries. Thereafter, isopropyl alcohol (IPA) is used to rinse off the methanol [3]. IPA is very hygroscopic, so it will leave the surface dehydrated. In many cases, an IPA-cleaned surface is equivalent to a dehydration-baked surface. At the end, the IPA liquid on the substrate surface is dried by blow-drying with clean, dry, and high-velocity nitrogen [3].

To dislodge tiny particles that could not be removed by rinsing or by blowing with nitrogen, the sonic cleaning is employed [3], see **Figure 12**. Ultrasound is a sound wave travelling through a medium at a frequency above 18 kHz. The ultrasonic cleaning is done by immersing the item being cleaned in a fluid (water or another appropriate solvent) and generating a high frequency acoustic wave in the fluid around the item being cleaned [3, 7, 8].

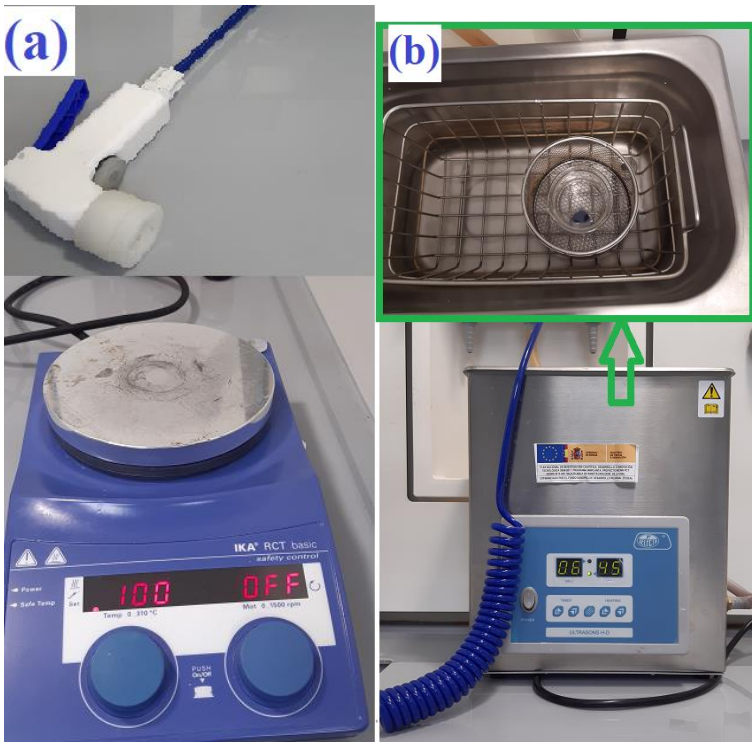

Figure 12: (a) the nitrogen spray and conventional hot plate, **(b)** the ultrasonic equipment in the cleanroom of university of Salamanca.

❖ Spin coating

A thin, uniform coating of photoresist at a specific, well-controlled thickness is accomplished by spin coating process. The resist film formation impacts on the outcome of the entire lithographic process as the film uniformity decides the exposure artifacts. To describe the fluid behavior during the spin coating, the whole process is divided into four stages:

1. Dispense,
2. Spread,
3. Thin-out, and
4. Evaporation [3].

Figure 13 depicts a spin coater, which is composed of a vacuum chuck on a motorized turntable. At the first stage of spin coating, a sufficient amount of polymer solution with a pipette is dispensed onto a wafer and thus a film is formed [3]. Then, at the second stage, the wafer is rotationally accelerated up to a preset speed. In the third

stage, the resist solution flows radially outward due to centrifugal force, and thus the fluid layer thickness reduces. At the last stage of spin coating, the continuous evaporation of solvent from the resist solution changes the fluid composition and thereby the rheological properties of the fluid [3].

Figure 13: Spin coater facility in the cleanroom of university of Salamanca.

❖ Post-Apply Baking

The drying process after spin coating in order to stabilize the resist film by reducing the extra amount of solvent is "post-apply bake (PAB)", also called a softbake or a prebake [6]. The post-apply bake can decide the properties of post-exposure and development processes. This is done by placing a wafer on the hot plate at a set temperature for a specific time. When the wafer is removed from the hotplate, baking continues as long as the wafer is hot. If an unbaked photoresist film is allowed to evaporate naturally at room temperature, it will lose solvent, albeit with changes in film properties. By doing the post-apply bake, there is a reduction in film thickness and improvement in adhesion. Moreover, it becomes less sticky and thus less prone to be contaminated by particulates [6].

❖ Exposure

In the "projection lithography" technique, an image of the mask is projected onto the wafer. The MJB4 Mask Aligner is a precision instrument for high-resolution optical lithography, widely being used in research laboratories, see **Figure 14**.

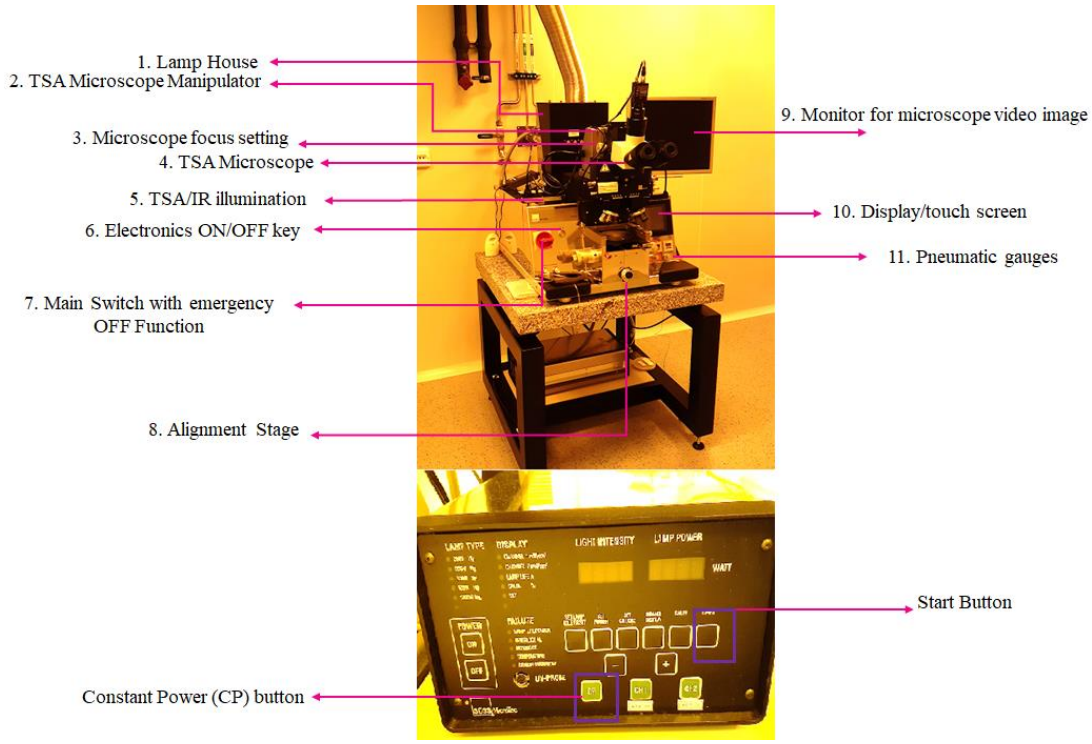

Figure 14: MJB4 mask aligner in the cleanroom of university of Salamanca.

During the photoresist exposure, one of the critical phenomena that we face with is the "standing wave effect", leading to the appearance of ridges in the sidewalls of the resist feature. The adverse effect of these ridges on the feature quality become more prominent as the pattern dimension gets smaller. The approach to reduce the standing wave effect is called "the post-exposure bake (PEB)" [6].

- **Post-exposure baking**

In general, PEB is applied to reduce the standing wave effect by baking at high temperatures ($100 - 130℃$). Indeed, the high temperature causes the diffusion of the photoactive compound of the resist, which makes the standing wave ridges smooth out [6].

- **Development**

Exposed photoresist becomes highly soluble in the developer. This property enables sharp vertical walls to be created even from diffused exposure profiles [3].

Generally, two types of developers are widely used in optical lithography: the metal hydroxide developers and tetramethylammonium hydroxide (TMAH) developers, also known as metal-ion-free (MIF) developers [3]. The former provides a constant pH during usage, with a wide process margin with a lower sensitivity to concentrations and temperature. But their metal ions are sources of contamination in some application, and they can also form salt deposits in the developer bowl [3]. While the latter does not suffer from the former drawbacks but their effectiveness is much more sensitive to changes in concentration and temperature [3]. A wafer can be developed by simply immersing it in a beaker.

- **Postbake**

To harden the final resist image, the postbake step is taken, aimed at

1. Cross-linking the resin polymer in the photoresist to make the image more thermally stable,
2. removing residual solvent, water, and gases, and
3. improving the adhesion of the resist to the substrate [6].

The postbake is usually taken at high temperatures (usually $120 - 150℃$). The postbake temperature is chosen by considering the glass transition temperature of the resist (a measure of its thermal stability), otherwise the resist will flow causing degradation of the image [6].

1.6 Annealing

Annealing as a step after patterning is done with the rapid thermal processor system, see **Figure 15**. Annealing process is also done on metal-semiconductor contacts to improve their properties after metallization [3].

The rapid thermal processor system is divided into two main parts:

1. the reactor and the associated circuits located in the upper part (process chamber, furnace, cooling circuit, gas panel and vacuum equipment), and

2. the control rack in the lower part (programmable logic controller, temperature controller, temperature sensor interface board, interface board for mass flow controllers, contactors, circuit breakers, transformer and power blocks).

Figure 15: The AS-ONE (RTP system).

1.7 Metallization

With the help of an electron-beam evaporator (See **Figure 16**), thin films of some desired materials are deposited on a substrate at a controlled rate. It consists of the following parts:

1. DC source,
2. Filament,
3. Beam current control circuits,
4. Crucibles,
5. Permanent magnets and electromagnets
6. Turbomolecular and scroll pumps

In this technique, a high vacuum (low enough pressure) is created with the help of turbomolecular pumps to provide a sufficiently long mean free path for the electrons to travel from the filament to the crucibles (filled with desired materials in the form of pellets) without collisions. A hot tungsten filament, held at strong potential ($-10\,kV$), generates a cloud of free electrons. The accelerated electrons tend to move away from the filament. Their direction is subjected to change due to the formed plates near the filament. Therefore, permanent magnets and electromagnets are needed to focus the electrons toward the center of the crucible. The small adjustments to the beam spot is done by the electromagnets. Moreover, they can be programmed to perform sweeps to cover a larger surface area [3].

Figure 16: The e-beam evaporator set-up in the cleanroom of the university of Salamanca. The substrate is adhered by Kapton tapes to the wafer shown in the figure and placed in the load-lock chamber. With the help of displacer, it is directed to the evaporation chamber during the process.

Deposition of a metal film on a semiconductor surface strongly depends on the following parameters [3]:

1. The metal type,
2. The semiconductor type (n-type/p-type),
3. Surface conditions, and
4. Annealing step after metallization.

Typically, two types of current-voltage (I-V) characteristics are expected for the metal-semiconductor contacts [3]:

1. Rectifying contact, and
2. Ohmic contact.

Indeed, the I-V characteristic depends on the type of the semiconductor (n-type/ p-type) as well as the relative position of the Fermi level of the semiconductor to the Fermi level of the metal [3]. Therefore, for an n-type silicon, in order to produce an ohmic contact, silver, aluminum and titanium are suitable metals. While gold, nickle and platinum are suggested metal contacts for a p-type doped silicon [3]. However, in reality, besides these theoretical assumptions, the roles of interface traps (in an extreme case leading to the Fermi-level pinning) and image force lowering should be taken into account [3]. Metal-semiconductor contacts are often annealed at elevated temperatures to improve their properties [3].

The film deposition is followed by a lift-off process. In this process, a patterned resist layer which is coated by a material is dissolved to “lift-off” the material that is on top of the resist [3]. In other words, the lift-off process is patterning the metal without etching [3].

1.8 Lift-Off

There are two main approaches used in the pattern transfer process, depending on the role of photoresist [3]:

1. to etch an underlying film, the photoresist is used as a chemical barrier (etch-down method);
2. to lift-off an overlying film, the photoresist is used as a soluble material (lift-off method).

Generally, the lift-off method consists of, see **Figure 17** [3]:

1. the photoresist film is spin coated, exposed and developed;
2. the film to be patterned is deposited on top of the photoresist using e-beam evaporation;
3. the photoresist is dissolved in solvent such as acetone. As the photoresist dissolves, the film above it will be released and float away and the remaining areas of the film will stay attached to the substrate.

Unlike the etch-down method, this method can be employed to pattern any metal or dielectric film [3]. In this method, it is of great importance that the solvent can penetrate the film to reach the underlying photoresist, through the inherent voids, cracks, and defects in the deposited film. This is immediately clear why it will be problematic if the film is either very thick or very conformal [3]. If the solvent due to the film thickness can not diffuse through it, then very rapid and cautious sonication of the solvent can help create microcracks in the top film [3].

The quality of the lift-off method strongly depends on the sidewall profile of the photoresist. Indeed, the presence of a gap between the film on the substrate and the film above the photoresist results in a clean lift-off, otherwise the film tearing is very likely to happen [3]. Among different film deposition techniques, thermal evaporation is the most desired one with the lift-off method [3].

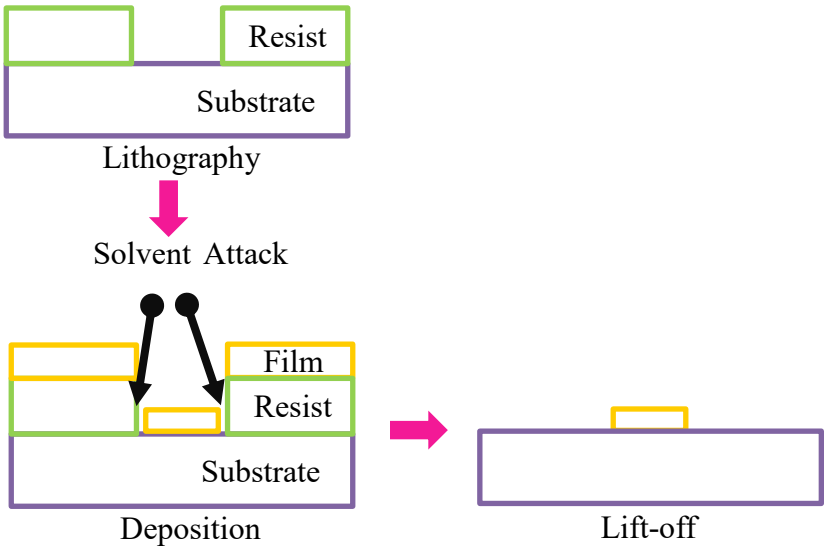

Figure 17: Lift-off patterning [3].

1.9 Exfoliation of 2D materials

Since the first successful exfoliation of monolayer graphene in 2004, different exfoliation techniques based on a common mechanical mechanism have been developed to obtain monolayer or few-layer flakes from layered bulk crystals to explore the properties of 2D materials. These techniques provide a platform to have high-quality yields of flakes at an extremely low cost in a laboratory scale (See **Figure 18**) [**9**].

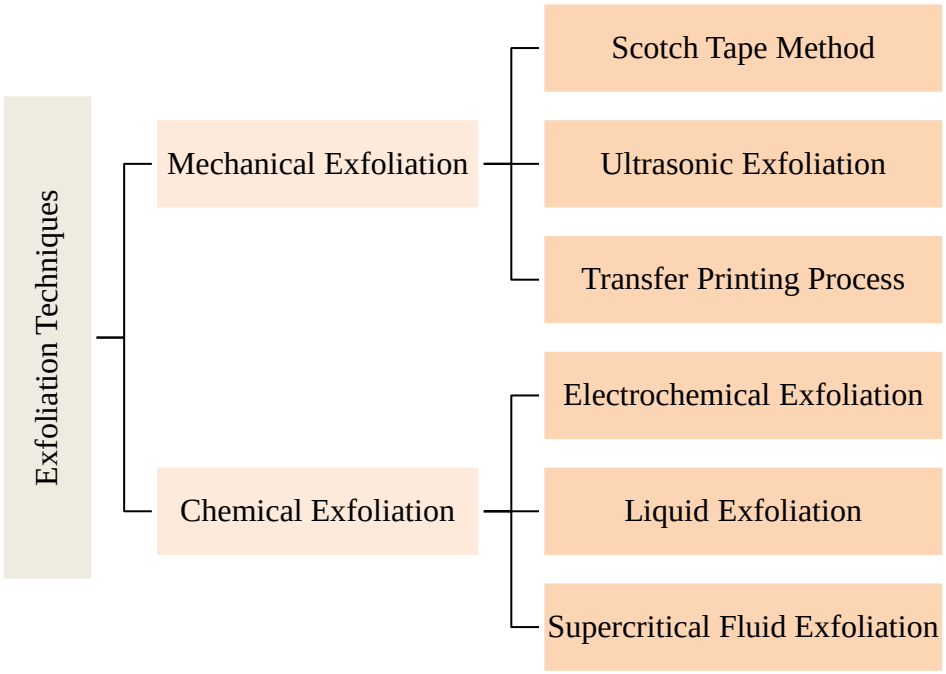

Figure 18: The exfoliation techniques [**7**].

In the conventional scotch tape method, the competition of van der Waals forces between the outermost sheet and a substrate governs the exfoliation technique. This technique comprises the following steps [**10**]:

1. the substrate is ultrasonically cleaned by an AMI cleaning approach,
2. thereafter, to remove ambient and organic adsorbates from the substrate surface, it undergoes the oxygen plasma cleaning,
3. following the plasma cleaning step, the desired-material-loaded tape is brought in contact with the substrate,

4. in the final step, the substrate with the attached tape is annealed for $2-5$ minutes at $100℃$ in air on a conventional laboratory hot plate. After the sample is cooled to room temperature, the adhesive tape is removed.

The time and temperature in the annealing step should be optimized, since increasing the annealing time and temperature leads to the negative effect of larger amount of glue residue distributed from the adhesive tape to the substrate surface. The suggested parameters for graphite exfoliation by Huang et al. [**10**] is $100℃$ for 2 minutes. The thickness of the resultant exfoliated flake is measured with Profilometer equipment, shown in **Figure 19**.

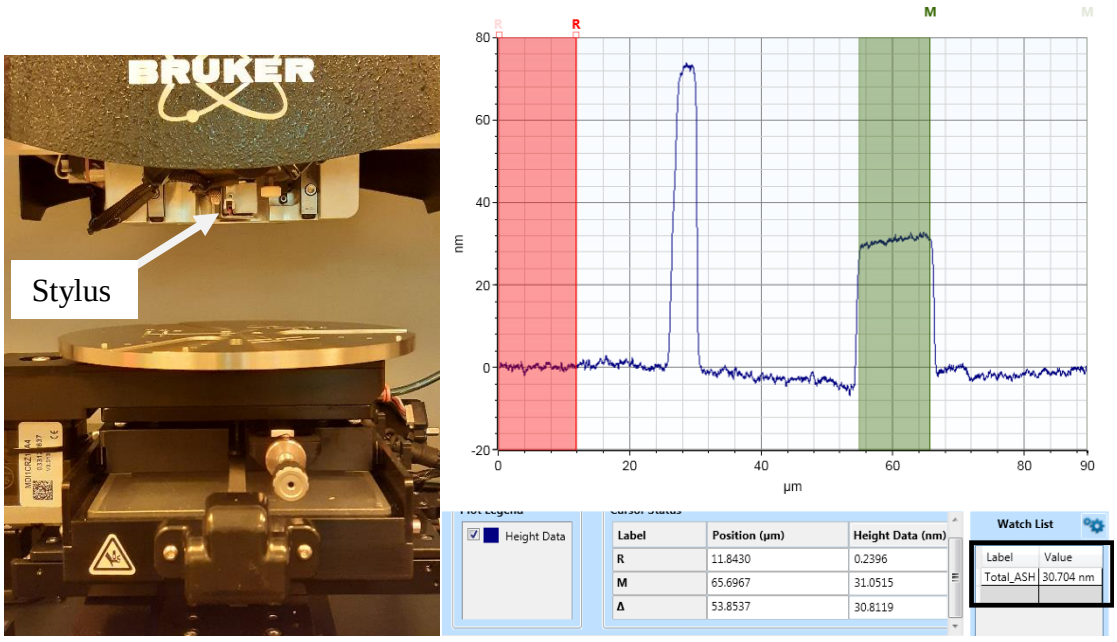

Figure 19: The Ptofilometer equipment and a result of the measured thickness of a flake.

❖ Scanning electron microscope (SEM):

To observe the topography of the surface of the exfoliated flakes, the scanning electron microscope (SEM) is used. In this characterization, an image is formed due to the detected secondary electrons by irradiating the surface of a specimen with a fine electron beam (or an electron probe) [**11**]. When a specimen is exposed to electron radiation, the scattering range of electrons inside the specimen depends on the electron energy, the atomic number of the elements making up the specimen and the density of the

constituent atoms [11]. **Figure 20** depicts the various emitted signals from the specimen after being impinged by an electron beam.

As depicted in **Figure 21**, the SEM equipment consists of the following parts:

1. an electron optical system to produce an electron probe including
    a) an electron gun,
    b) a condenser lens, and an objective lens to produce an electron probe,
    c) a scanning coil to scan the electron probe,
2. a specimen stage to place the specimen,
3. a secondary-electron detector to collect secondary electrons,
4. an image display unit, and
5. an operation system to perform various operations.

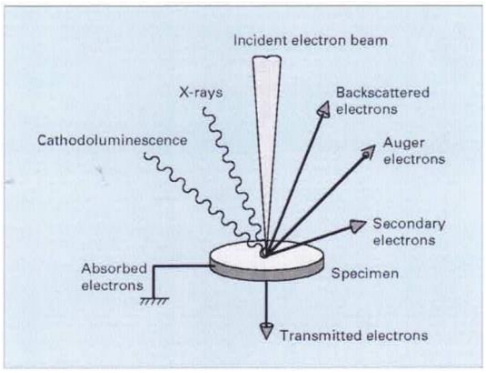

Figure 20: Emissions of various electrons and electromagnetic waves from the specimen [11].

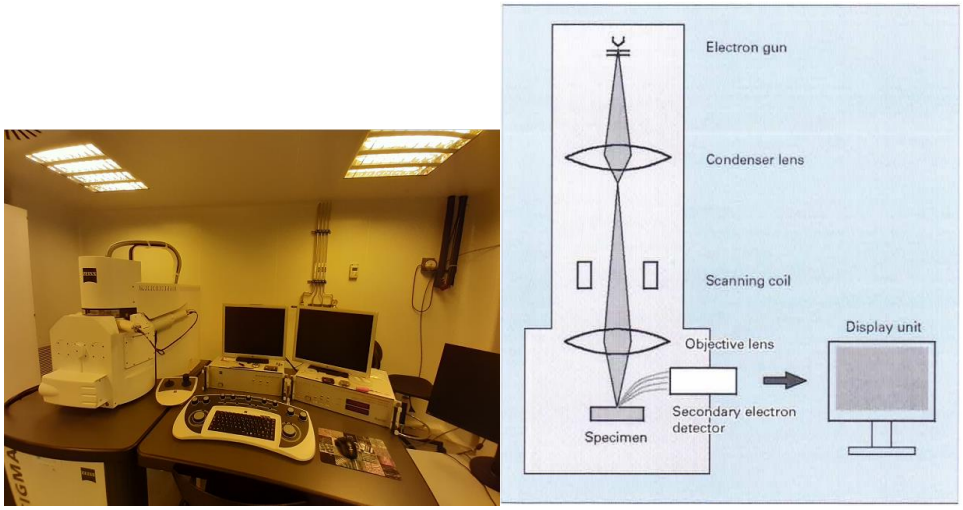

Figure 21: SEM equipment and its basic construction [11].

1.10 Hall-bar device Fabrication

In this thesis, the Hall-bar configurations are fabricated on the exfoliated flakes of $Pb_{0.77}Sn_{0.23}Se$ already transferred on the substrates of (Si/Si_2O), already patterned with markers. Briefly, the following steps were taken to fabricate a Hall-bar device:

1. Patterning gold markers on (Si/Si_2O) wafers through optical lithography and lift-off process of (titanium/gold)-deposited films (See **Figure 22**);
2. Ultrasonically washing the resultant wafers with the AMI cleaning approach, followed by O_2 plasma cleaning (See **Figure 23**);
3. exfoliation of the desired material and transferring them from the tape on the substrates with markers, fabricated in the last step (See **Figure 24** and **Figure 25**);
4. Designing a Hall-bar configuration with a CAD software (Elphy plus) matches the dimensions of the exfoliated flake;
5. electron-beam lithography for patterning the designed Hall-bars, followed by etching process; the spin coated resist is PMMA
6. deposition of $10nm/60nm$ (Titanium/Gold) films for the contacts; titanium takes the role of an adhesion layer whereas gold is a seed layer;
7. lift-off process (See **Figure 26**);
8. mounting the prepared device on a sample holder using silver paste;
9. bonding the contacts of the prepared device to the legs of the sample holder.

The 15 $seconds$ etching recipe for the exfoliated flakes of $Pb_{0.77}Sn_{0.23}Se$ in this study is as follows:

- CHF_3 flow rate of 15 sccm, and
- Ar flow rate of 35 sccm,
- with the ICP power of 600 W at 13.56 MHz, and
- RIE power of 60 W at 13.56 MHz, DC Bias (167 V)
- at pressure 6 $mTorr$ and strike at 6 $mTorr$
- at 20℃ recirculator temperature,

- with backside Helium pressure 10 Torr.

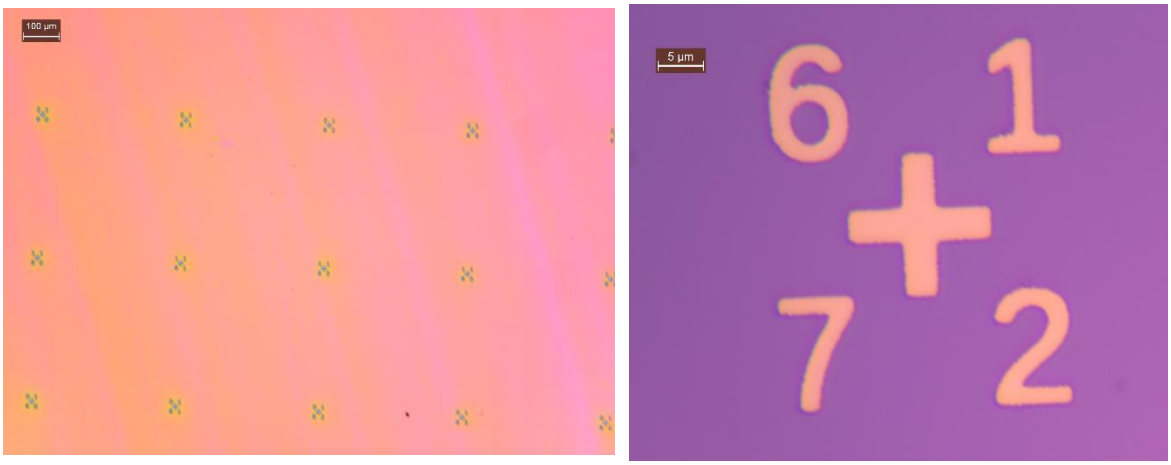

Figure 22: the marker patterns on the Si/Si_2O substrate.

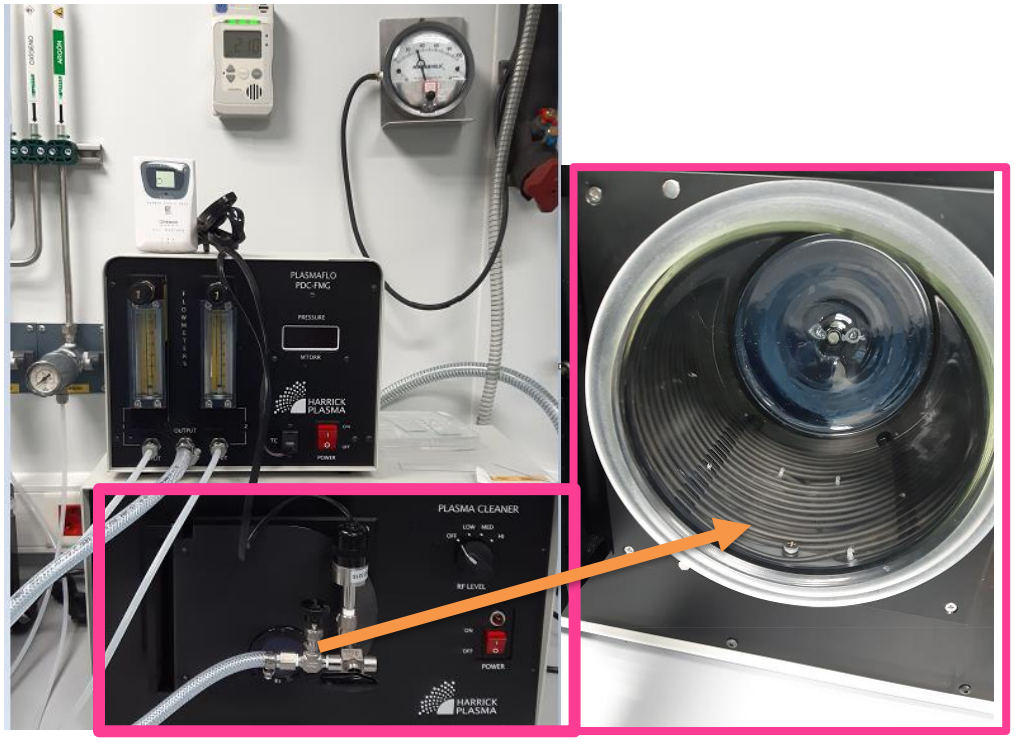

Figure 23: The Plasma cleaner equipment being used in the cleanroom of university of Salamanca.

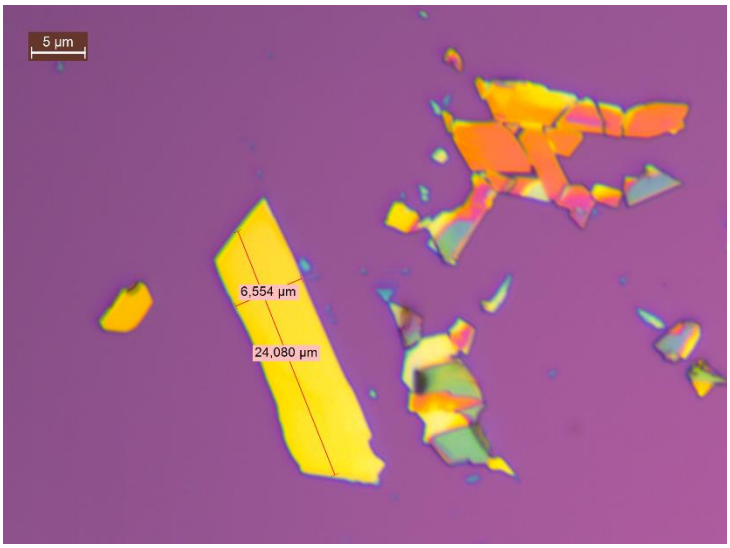

Figure 24: The image of a $Pb_{0.77}Sn_{0.23}Se$ flake.

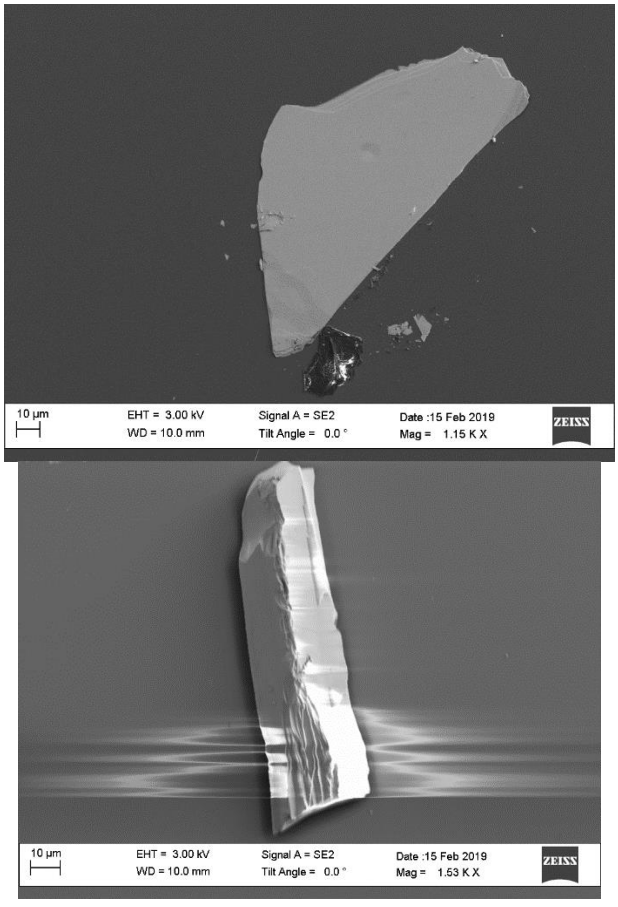

Figure 25: The SEM image of $Pb_{0.77}Sn_{0.23}Se$ flakes.

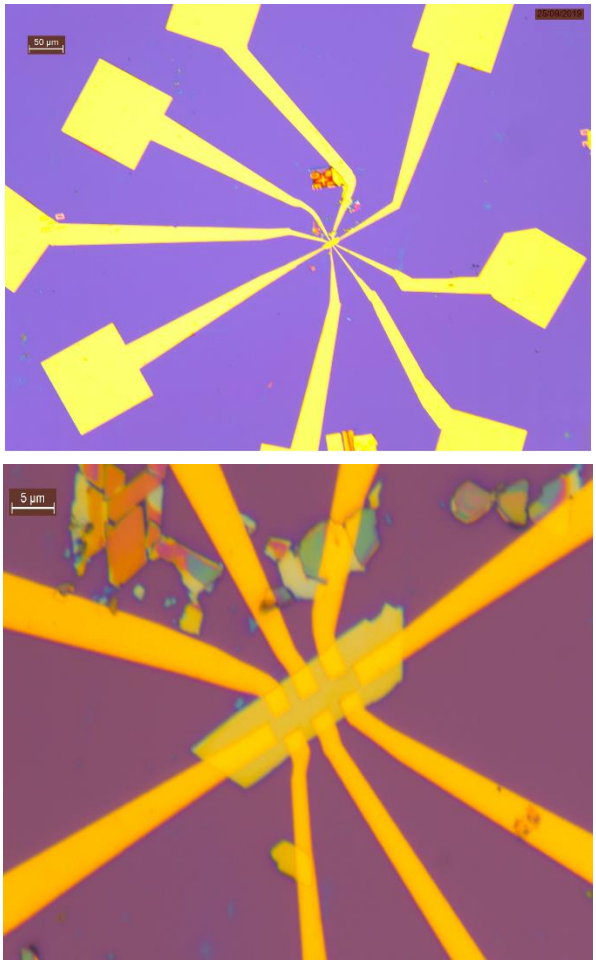

Figure 26: The microscopic image of $Pb_{0.77}Sn_{0.23}Se$-based Hall bar devices after lift-off process.

1.11 Raman Spectroscopy

For the first time, the inelastic scattering of light by a fluid is demonstrated by Sir C. V. Raman and K. S. Krishnan [12]. This discovery and later instrumental innovations bring about a revolution in Raman spectroscopy technique, so that nowadays the sample sizes and measuring times are drastically reduced [12]. In today's research, Raman spectroscopy is a relatively fast method and well-suited technique to investigate solids, liquids, solutions and even gases depending on the experimental setup used. Micro-Raman spectroscopy is one of the rare spectroscopic methods enables us to obtain molecular information at the micrometer scale [12].

The inelastic scattering of electromagnetic radiation is explained with the Raman effect. The energy transfer between the photons and the molecular vibrations during this interaction, accounts for the different energies of the incoming and the scattered photons [12]. Indeed, when a molecule is positioned in an electrical field $\vec{E}$ (caused by electromagnetic radiation), an electrical dipole moment $\vec{P}$ is induced, given by

$$\vec{P} = \alpha . \vec{E} \tag{1.4}$$

where α is polarisability, dependent on the shape and dimensions of the chemical bond. As chemical bonds change during vibrations, the polarisability is dependent on the vibrations of the molecule [12]. Moreover, light can be considered as an oscillating electrical field [12] described by

$$\vec{E} = E_0 Cos(2\pi . \nu_0 . t) \tag{1.5}$$

where ν_0 is the vibrational frequency of the electromagnetic radiation [12]. Therefore, the induced dipole moment as a function of the vibrational frequencies of the molecule ν_V and of the incident radiation ν_0 can be split into 3 components, each with a different frequency-dependency, given by

$$\vec{P} = \vec{P}(\nu_0) + \vec{P}(\nu_0 + \nu_V) + \vec{P}(\nu_0 - \nu_V) \tag{1.6}$$

The first term corresponds to the elastic scattering of the electromagnetic radiation [12], where the induced dipole moment has the same frequency (hence the same energy) as the incoming radiation, called “Rayleigh scattering”. The second and the third terms correspond to the inelastic scattering of light: “Raman scattering”. The second term corresponds to a higher energy of the scattered radiation, compared to the incident beam (Anti-Stoke scattering), while the last term represents a lowering of the frequency (Stoke scattering) [12].

In order to take the fingerprint of materials using Raman spectroscopy, an intense monochromatic beam of electromagnetic radiation (usually a laser) is focused on the sample, and the intensity of the scattered radiation is measured as a function of its wavelength [12]. Usually, in a Raman spectrum the intensity is plotted as a function of

the Raman wavenumber ω expressed in cm^{-1}, which is related to the difference in frequency between the scattered light and the incident electromagnetic radiation:

$$\omega = \bar{\nu}_m\text{-}\bar{\nu}_0 = \frac{\nu_m}{C} - \frac{\upsilon_0}{C} \quad (1.7)$$

where ν_m and ν_0 are the frequency of the scattered (measured) and incident radiation, respectively; and c is the speed of light [12]. Wavenumbers are usually expressed in cm^{-1}; positive wavenumbers correspond with Stokes scattering and negative wavenumbers correspond with anti-Stokes scattering [12].

According to Schrodinger equation, only a limited number of energy levels are allowed

$$E_\nu = \left(\nu + \frac{1}{2}\right).h\nu_\nu \ (\nu = 0, 1, 2, \dots) \quad (1.8)$$

where ν the vibrational quantum number, h Planck's constant ($h = 6.63 \times 10^{-34} J.s$) and ν_ν the vibrational frequency. During the transition of one vibrational level to the next, the difference in quantum numbers between begin and end state should equal 0 or ± 1 [12].

As depicted in **Figure 27**, if the difference equals 0, Rayleigh scattering occurs, otherwise Stokes or Anti-Stokes (Raman) are the desired cases. Therefore, it can be inferred that the overall energy difference for a Raman transition equals with $\pm h.\nu_\nu$. This energy difference is plotted on the horizontal axis of a Raman spectrum, expressed as Raman wavenumbers. The position of a Raman band in the spectrum is determined by the energy difference between the ground state and the first vibrationally excited state [12].

Every commercial Raman spectrometer consists of four major components (See **Figure *28***) [13]:

1. Excitation source which is generally a continuous wave (CW) laser,
2. sample illumination and collection system,
3. wavelength selector, and
4. detection and computer control/processing systems.

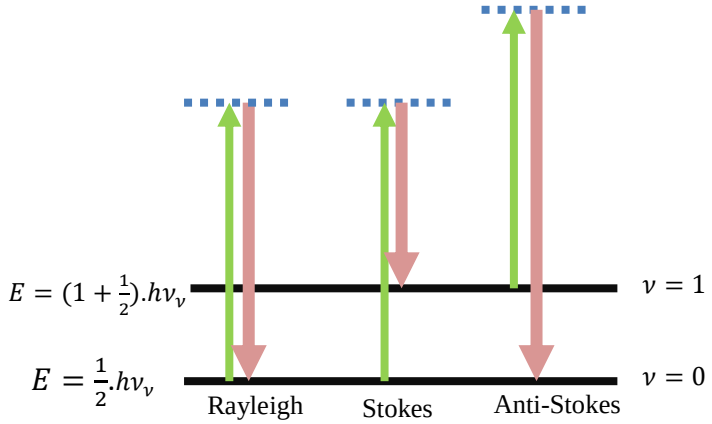

Figure 27: Idealized model for the dispersion of light by molecules [12].

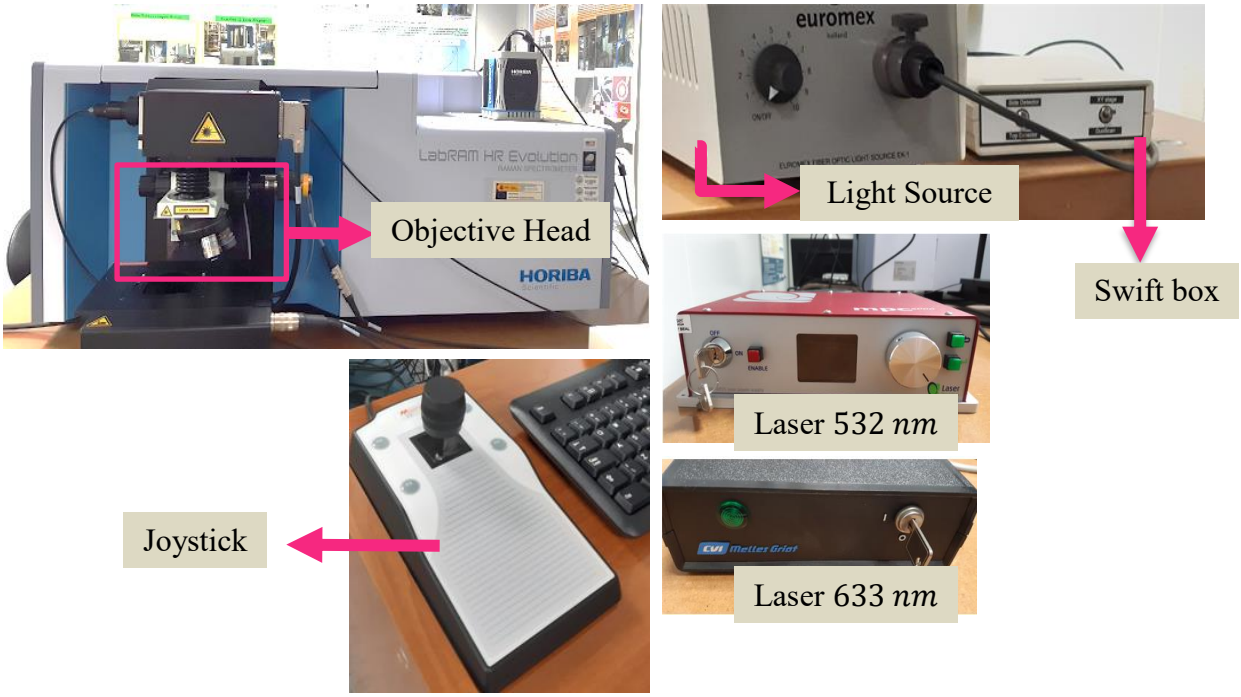

Figure 28: The Horiba Labram Raman Spectroscopy set-up in the university of Salamanca.

1. 12 Cryogenic engineering

The word ***Cryo-*** originates from the Greek *Krous*; meaning icy cold. The cryogenic engineering and involved technologies are not fundamentally different than refrigeration, defined as "to make things cold". Temperature below -150℃ (123.15 K) are known as the Cryogenic temperatures, covering the normal boiling point of most

gases (except for the so-called permanent gases including hydrogen, oxygen, nitrogen, carbon monoxide and the inert gases) [14]. Liquefaction of three of these permanent gases (oxygen, nitrogen and hydrogen) as well as the invention of a double-walled glass flask to preserve the cryogens with the aim of minimizing the heat exchange between the cryogen and its container paved the way for helium liquefaction and the birth of "low temperature science" [14].

Helium ($_4$He) belongs to the family of inert gases, with the lowest boiling temperature in this family. The basic physical properties of Helium are tabulated in **Table II**. **Figure 29** shows the phase diagram of helium ($_4$He).

Table II. Basic Physical properties of Helium [14].

Basic Physical Properties of Helium	
Symbol	He
Atomic Number	2
Atomic Mass	4.0026 *amu*
Normal Boiling Point	4.216 K

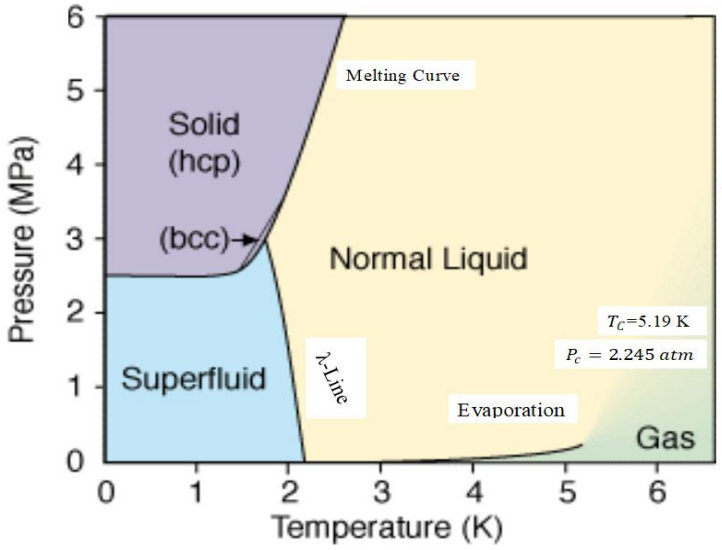

Figure 29: Phase diagram of $_4$He, figure is from [14].

Helium due to its low boiling point is the lifeblood in low-temperature physics, while it is scarce and non-renewable natural resource. Therefore, the growing unbalance between its supply and demand has raised serious concerns over resource shortage, higher price, etc, leading to the development of cryo-coolers as solutions [14]. **Figure 30** shows some helium applications [14].

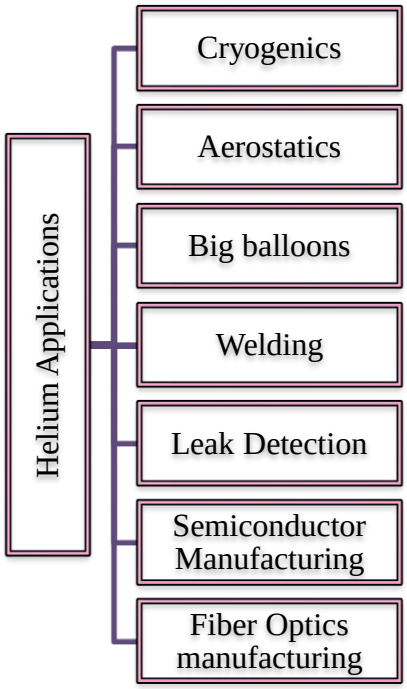

Figure 30: Helium Applications [14].

1. 13 4 *K* Regenerative Cryocoolers

A cryocooler is a mechanical device that recirculate a refrigerant through a refrigeration cycle, producing continuous low temperatures below $123\ K$. A cryocooler system consists of a compressor, a cold head (expander), and helium hoses to transfer pressurized helium gas to the cold head from the compressor [14]. All mechanical cryocoolers generate cooling by expanding a gas from a high pressure to a low pressure, called "Simon Expansion" process [14]. The nature of the refrigerant flow within the cryocooler decides the type of the cryocooler:

- alternating flow (AC system) or
- continuous flow (DC system) [14].

This classification also determines the applicable type of heat recovery heat exchanger

- Regenerators for an alternating flow (AC system) or

- Recuperators for a continuous flow (DC system) [14].

A regenerative heat exchanger in the regenerative cryocooler is called a "regenerator", performing like a thermodynamic sponge in a cycle; while a heat exchanger in the recuperative cryocooler is called a "counter flow heater exchanger" [14].

As depicted in **Figure 31**, the regenerative cryocoolers are divided into two main groups: valveless and valved systems. The stirling cryocooler and stirling-type PT cryocoolers are valveless systems (without rotary valve) [14].

On the other hand, Gifford-McMahon (GM) and GM-type PT cryocoolers belong to the valved cryocooler class. The main components of these two classes are [14]:

1. A constant DC-flow compressor package,
2. cold head including:
   a) switching valves (or a rotary valve),
   b) regenerator,
   c) cold-end heat exchanger,
   d) displacer, and
   e) displacer drive
3. supply and return stainless steel (SS) flexible lines,

The connection role between the compressor and the cold head is taken by supply and return stainless steel (SS) flexible lines. Moreover, as the compressor is a DC-flow device, it can be located remotely from the cold head from few meters to few hundred meters [14]. The Switching valves (or a rotary valve) chop the DC gas flow into a periodic oscillating gas flow (also called AC flow) within the cold head itself. Both GM and GM-type PT cryocoolers normally operate with pulsation frequencies of $1 - 2.4\ Hz$ [14]. With these low operating frequencies, the two-stage cryocooler has better efficiencies at low temperatures, especially with the discovery of rare earth regenerator materials with higher specific heat at temperatures below $10\ K$ [14].

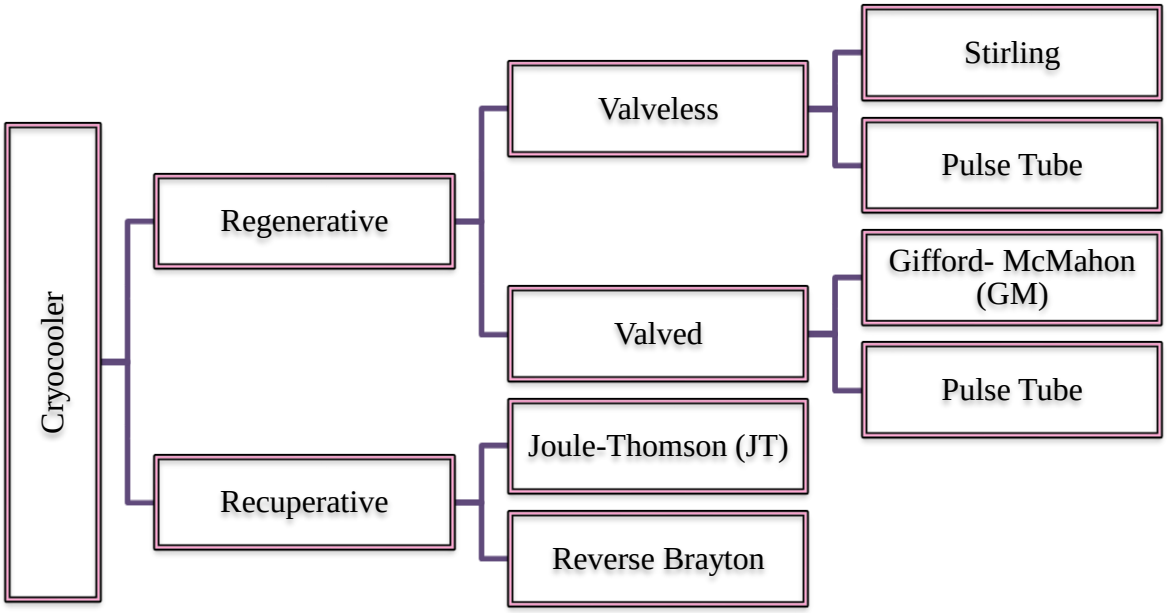

Figure 31: Classification of commercial cryocooler [14].

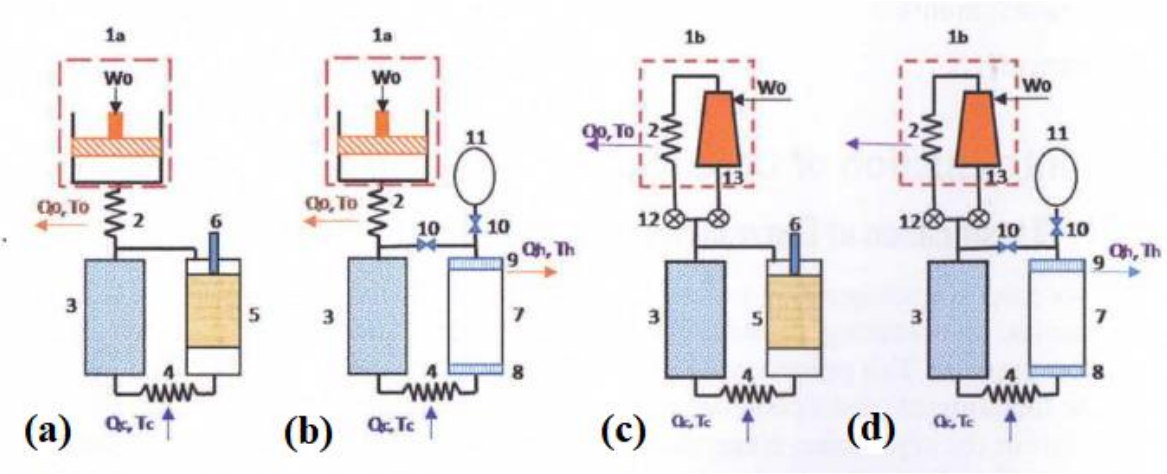

Figure 32: Regenerative Cryocoolers: **(a)** Stirling cryocooler, **(b)** Stirling-type PT cryocooler, **(c)** GM cryocooler. **(d)** GM-type PT cryocooler. (1a) Valveless compressor, (1b) Valved compressor package, (2) Warm-end heat exchanger, (3) Regenerator, (4) Cold-end heat exchanger, (5) Displacer, (6) Displacer drive (mechanical or pneumatical), (7) Pulse tube displacer (also called "pulse tube"), (8) Cold-end flow straightner, (9) Warm-end flow straightner, (10) Orifices and/or inertance tubes, (11) Gas reservoir, (12) Switching Valves (rotary valve), (13) DC flow compressor module. Figure is from [14].

1.13.1 Compressor Package

The GM-cryocoolers benefit from their potential to work with commercially available, relatively inexpensive, oil-lubricated compressor modules used in air conditioning for the compression part of the cycle. Moreover, the operation of these oil-lubricated compressor modules relies on two of their components, an efficient oil separator and an adsorber to keep oil out of the cold head. The oil takes the role of lubrication and cooling in the compressor module. **Figure 33** shows a flow diagram of a water-cooled compressor package and its major components. It is evident that three flow loops determine its working principle, namely helium gas, oil and cooling water [**14**].

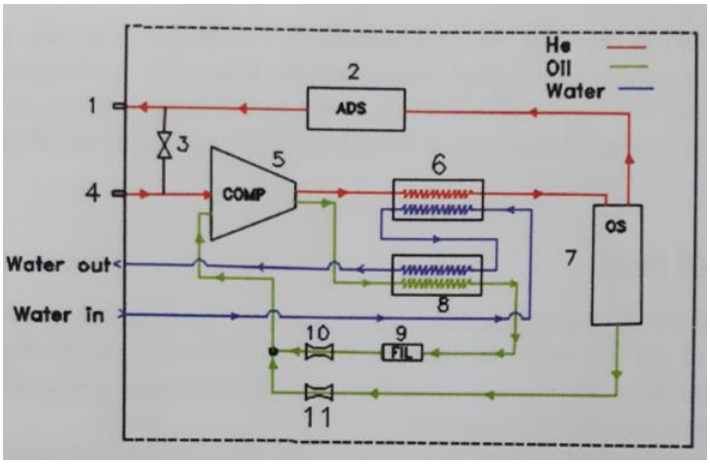

Figure 33: Flow diagram of a DC flow compressor package: (1) Aeroquip connector for HP gas, (2) Adsorber, (3) Bypass valve, (4) Aeroquip connector for LP gas, (5) Compressor module, (6) Aftercooler (I) (gas), (7) Oil separator, (8) Aftercooler (II) (oil), (9) Filter, (10-11) Orifices. Figure is from [**14**].

1.13.2 **GM-Pulse Tube Cold Head**

Similar to the GM-cryocoolers, the PT-cryocoolers employ the compressor and rotary valve. The design of the pulse tube and thus the efficiency of the cycle is of great importance to avoid the formation of the convective heat transfer loops [**14**]. The PT cold head could be designed in three configurations [**14**]:

1. U-type (See **Figure 34** (a));
2. Coaxial-type (See **Figure 34** (b));

3. Inline-type

The two-stage PT cryocooler are divided into two categories: standard and remote motor, See **Figure 35**. In the standard version, the rotary valve/motor assembly is located at the warm end of the pulse tube cold head; while in the remote version as the name implies, the rotary valve/motor assembly is separated from the PT expander [**14**].

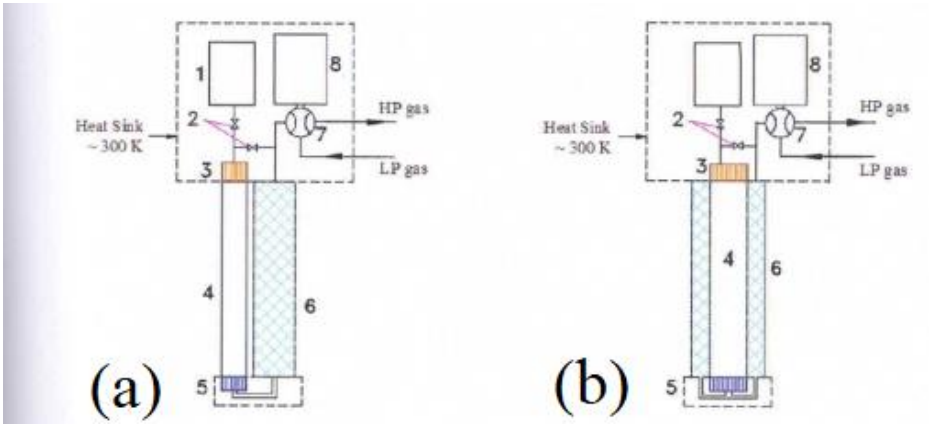

Figure 34: Two practical designs of a PT cryocooler: **(a)** U-type design, **(b)** Coaxial design. (1) Reservoir, (2) Orifices, (3) warm-heat exchanger, (4) Pulse tube, (5) Cold-heat exchanger, (6) Regenerator, (7) Rotary valve, (8) Motor. Figure is from [**14**].

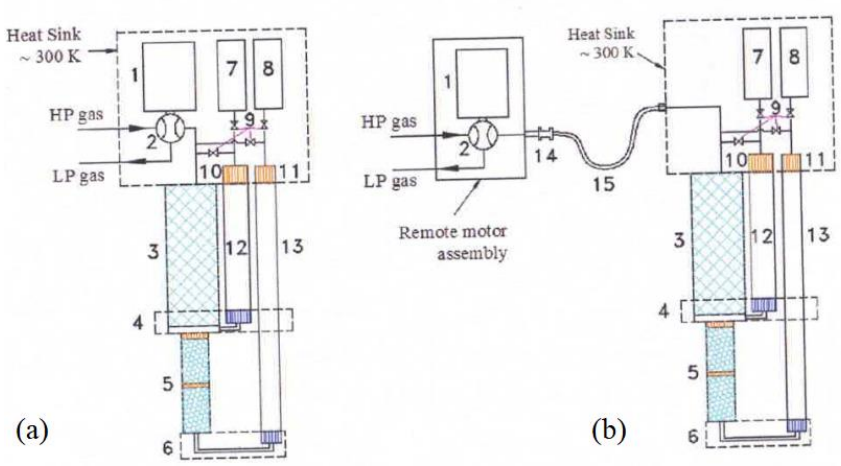

Figure 35: Schematic of a two-stage PT cryocooler: (a) Standard, (b) Remote motor. (1) Motor, (2) Rotary Valve, (3) First-stage regenerator, (4) First-stage heat exchanger, (5) Second-stage regenerator, (6) Second-stage heat exchanger, (7, 8) First- and second-stage reservoirs, (9) Orifices, (10-11) First- and second- stage warm-heat exchangers, (12-13) First- and second- stage pulse tubes, (14) Electrical isolator, (15) Remote motor line. Figure is from [**14**].

1.14 Superconducting Magnets

The efficiency of a superconductor is determined by three critical parameters (critical temperature, critical field and critical current density). A superconducting magnet is supposed to perform below the surface of these three parameters (See **Figure 36**). A transition to resistive state or "quench" will occur, once the magnet operates above this surface [**14**].

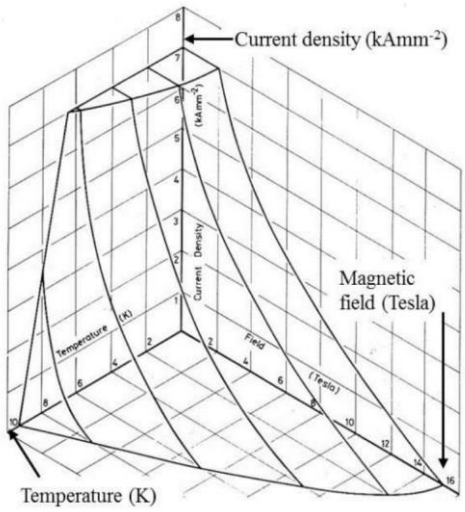

Figure 36: Critical current surface of superconducting alloy NbTi [**14**].

1.14.1 Quench Protection

It is said that a superconducting magnet quenches either it goes beyond its superconducting limits (wire's critical limit of field and/or current), or one exceeds the critical temperature surface. The temperature rise in a superconducting wire is explained by the following reasons [**14**]:

1. Frictional heating within the winding pack due to a small wire movement,
2. eddy currents or hysteresis loss in the superconductor during charge or discharge of the magnet,
3. Magnet warming due to a loss of system vacuum, or

4. loss of cooling power (when power is lost to the cryo-refrigerator compressor or when a cryo-cooler failure occurs).

There are two common quench protection approaches known as active or passive quench protection (See **Figure 37**) [**14**].

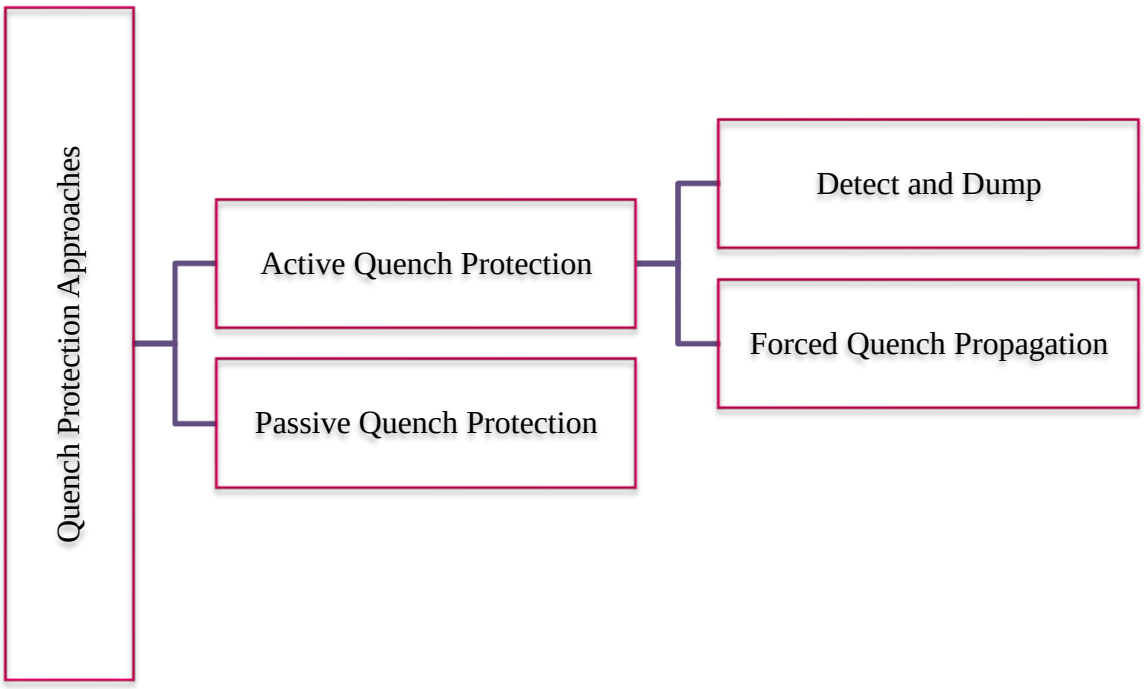

Figure 37: Quench Protection Approaches [**14**].

Active quench protection technique: it refers to protection of a magnet using active (usually externally driven) means. Generally, there are two types of active quench protection techniques to prevent possible damage, based on detection of the quench onset and managing the released magnet energy [**14**]:

1. Detect and Dump
2. Forced quench propagation

In the "detect and dump" technique, it is of great importance to detect the onset of quench very rapidly to dissipate the quench energy through a resistor branch, which is in parallel with coil. For this reason, the voltage taps are distributed at strategic locations in the coil to monitor the voltages during charging and subtract the inductive terms from the resistive terms to find out the onset of the quench. Any recorded voltages crossing the

threshold value makes the relay connected and the dump resistor be in the circuit to dissipate the current. Simultaneously, the power supply will be stopped supplying current to the magnet (See **Figure 38**) [**14**].

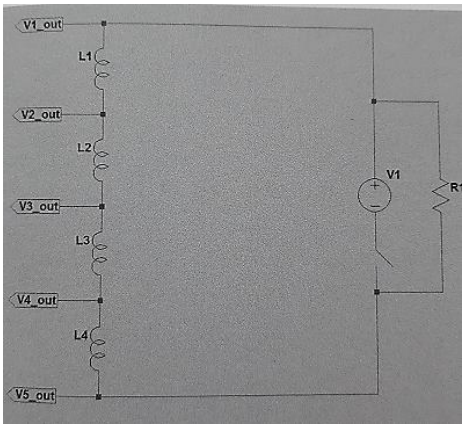

Figure 38: Active quench protection diagram [**14**].

Passive Quench Protection technique: most small-scale laboratory magnets benefit from this technique, which is based on the self-protection of the magnet during a quench. To meet this goal, among variety of choices of a superconductor, the proper one is the copper content of the wire. Moreover, to take control of the voltage drop over the winding pack, the coil is divided into inductive sections with bypass diodes and resistors, with a maximum threshold voltage for every section. **Figure 39** depicts a typical passive quench protection system using subdivision only with diodes. The operation of this circuit during a quench is as follows: as the quench propagates, an inductor in series with a resistor (with an increasing value) is an equivalent section for an inductor section. Therefore, the voltage drop over the resistor continuously increases until it can turn on the diode and allow the current to bypass the resistive section. Moreover, due to the thermal avalanche resulting from the close thermal contacts of coil subsections, the quench energy is distributed. At this moment through recorded changes of a current or voltage, the power supply must stop supplying the current flow to the diodes and magnet very immediately. Apparently, it is fairly challenging to find a diode that function reliably at high current (beyond the operating current of the magnet), at cryogenic temperature and in high magnetic fields, with ability to handle rapid thermal changes.

Moreover, the metal film resistors are suitable options to operate at cryogenic temperatures (in case the resistors are used in series with the diodes) [14].

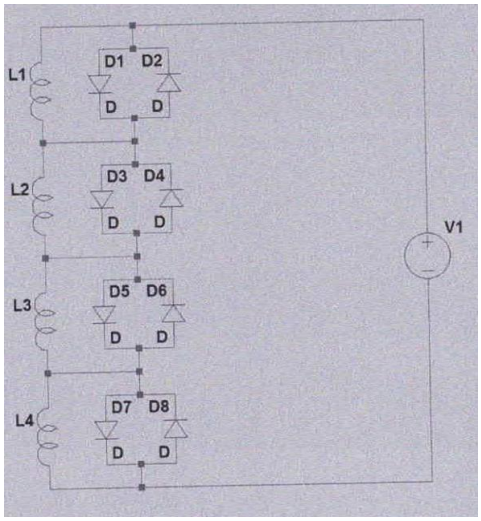

Figure 39: Passive quench protection diagram [14].

1.15 TeslatronPT refrigerator (PTR)

Teslatron pulse tube refreigerator (PTR) (see **Figure 40**) belongs to the standard two-stage GM-PT cryocooler class, with the main following parts [15]:

1. cryostat, including PTR cold head, variable temperature insert (VTI) and superconducting magnet,
2. compressor for PTR,
3. gas handling system for the VTI, including sealed circulation pump and $4He$ gas storage vessel,
4. top loading sample probe,
5. electronics rack including
    - Mercury iPS power supply for magnet control and monitoring the PTR temperatures,
    - Mercury iTC temperature controller to monitor and control the VTI and sample probe.

The VTI main role is to adjust the temperature of a sample over a wide range, typically between $1.5\ K$ and $300\ K$. The VTI is vacuum insulated from its surroundings

which is in common with the cryostat vacuum. The control tube of the VTI is known as the sample space, filled with $4He$ to give good thermal contact between the sample and the VTI heat exchanger. The sample is mounted on a top loading probe which is inserted into the central tube of the VTI via an NW50 flange on the cryostat top plate [15]. The superconducting magnet in Teslatron benefits from the passive quench protection [15].

Figure 40: Teslatron pulse tube refrigerator.

1.16 Low-Power Measurement Methods

The low-power device characterization operating with very small currents and voltages are commonplace in research laboratories; like the measurement of resistance and I-V characteristics of nanowires, nanotubes, semiconductors, metals, superconductors and insulating materials. In these measurements, it is of great importance to keep the noise level minimized. In this regard, two very popular AC measurement techniques in laboratories are [16]:

1. a lock-in amplifier; to apply a low level AC current to the sample and measure its voltage drop;
2. a DC current reversal technique.

In both methods, DC noise and the noise at higher frequencies are rejected [16]. In sensitive I-V and resistance measurement instruments, there are two main parts:

1. The Current Source,
2. The Voltage Measurement Instrument.

In the lock-in method, the AC current source should be constructed by applying a voltage over a resistor. While in the DC reversal method, a current source with reversible polarity is used, and the sample response is measured with a nanovoltmeter [16].

1.16.1 Lock-in Amplifier method

Figure 41: Lock-in amplifier model SR830 equipment.

Lock-in amplifiers are electrical instruments capable of extracting signal amplitudes and phases in extremely noisy environments (See **Figure 41**). The working principle of this instrument, to measure a signal's amplitude and phase relative to a periodic reference, is based on the demodulation (phase sensitive detection) by [16]

1. a homodyne detection scheme, and
2. low-pass filtering

The extracted signal is singled out at a specific reference frequency and phase, while other frequencies are rejected [16].

The operation of a lock-in amplifier strongly depends on two controllable parameters, the time constant and the dynamic reserve. In every lock-in amplifier, there is

at least a low-pass filter. This filter can be controlled with its time constant; for this reason, there is a time constant display compartment on the front panel. The trade-off between the responsiveness and stability is done by adjusting the time constant while changing input or taking measurement. Therefore, for very low time constants, the voltage reading is non-stable but very fast. While, the opposite happens for the high time constants. The dynamic reserve is defined as the largest tolerable ratio of noise to signal and can be adjusted on the panel from high to low. As a rule, the dynamic reserve should be kept as low as possible without overloading [**17**].

To measure the voltage of a sample at low power with the lock-in technique, current is forced through the sample by applying a sinusoidal voltage across the series combination of R_{REF} and the sample. Usually, R_{REF} is chosen to be much larger than the sample resistance, thereby creating an approximate current source driving the sample. The amplified voltage from the sample is multiplied by both a sine and a cosine wave (with the same frequency and phase as the applied source) and then put through a low pass filter. The outputs of the low pass filters are the real (in phase) and imaginary (out of phase) content of the voltage at the frequency f_0. It is often chosen that the instrument operate at a relatively low frequency (less than 50 Hz). A low frequency is chosen for many reasons. These include [**16**]

1. Getting far enough below the frequency roll-off of the sample and interconnects for an accurate measurement,
2. Avoiding noise at the power line frequency,
3. Getting below the frequency cutoff of in-line electromagnetic interference (EMI) filters added to keep environmental noise from reaching the sample.

DC Reversal Measurement Method: An alternative to lock-in amplifier uses DC polarity reversals in the applied current signal to nulify noise. This is a well-established technique for removing offsets and low frequency noise. In this technique, one simply applies a current to the sample and measures the sample voltage, then reverses the current and remeasures the voltage. The difference of the two measurements divided by two is the voltage response of the sample to the applied current level.

Repeating the process and using averaging reduces the noise bandwidth and therefore the noise. These are called “Delta” measurements [16].

1. 17 Summary

The fabrication and characterization ideas explained in this chapter are the ones which are used to fabricate and characterize Hall bar devices in the following chapter. Next chapter deals with Raman characterization of exfoliated flakes of $Pb_{0.77}Sn_{0.23}Se$ at different experimental conditions. Furthermore, the Hall-bar configurations fabricated on $Pb_{0.77}Sn_{0.23}Se$ flakes are characterized at low temperatures mounted in Teslatron cryostat, with the lock-in technique.

Chapter 2 Topological Insulators

"I don't have any particular recipe. It is the reason why doing research is challenging as well as attractive. It is like being lost in a jungle and trying to use all the knowledge that you can gather to come up with some new tricks, and with some luck, you might find a way out".

Maryam Mirzakhani

2.1 Introduction to Topological Insulators

The phases of materials (gas, liquid, solid, magnet, superconductor, …) are determined by the arrangement of atoms and electrons and thus associated with different symmetries according to Landau's symmetry-breaking theory [**18**]. Unlike most other phases, topological insulating phases were first proposed theoretically and then observed experimentally and determined by global symmetry breaking [**18**, **19**]. The designation of topological insulators (TIs) is explained with the fact that they are insulators in the "bulk" but with exotic metallic states present at their surfaces owing to the topological order [**20**].

In a normal insulator, the bandgap E_{gap} between the empty conduction band and fully occupied valence band is so large. Therefore, at room temperature the completely filled bands can not contribute to the carrier transport and thus the material is insulating. The same scenario works for an intrinsic semiconductor, but due to its smaller bandgap the carriers have the chance to get thermally excited from the valence into conduction band [**21**]. In contrast, as depicted in **Figure 42**, in three-dimensional (3D) TIs, surface states, with a linear dispersion crossing each other at the so-called Dirac point, exist within the bandgap [**21**]. The linear dispersion makes the electrons behave like massless relativistic particles. These surface states are helical, meaning that the spin orientation is locked to the direction of motion, leading to the carrier transport with suppression of backscattering, since it is unlikely that both the direction of propagation as well as the spin orientation get inverted [**21**]. Therefore, this intrinsic property based on the spin-orbit coupling (SOC) mechanism provides a promising platform for spintronic applications [**20, 21**]. SOC is the quantum magnetic field inside an atom of a Kramer's system having spin-orbit interactions which induced a transverse magnetic force on an orbiting electron in the external electric field created by the charge of the nucleus [**18**]. This relativistic quantum mechanical effect arises from the relativistic momentum dependent motion of the charged particle into the electric field of the atom [**18**]. The similarity between the surface state of TIs and graphene is that they both have Dirac electronic structure; although the surface state of TIs has one Dirac point (or valley) and

no spin degeneracy, whereas graphene surface has two Dirac points and is spin degenerate. This difference leads to distinguishing applications for TIs in quantum computing [20].

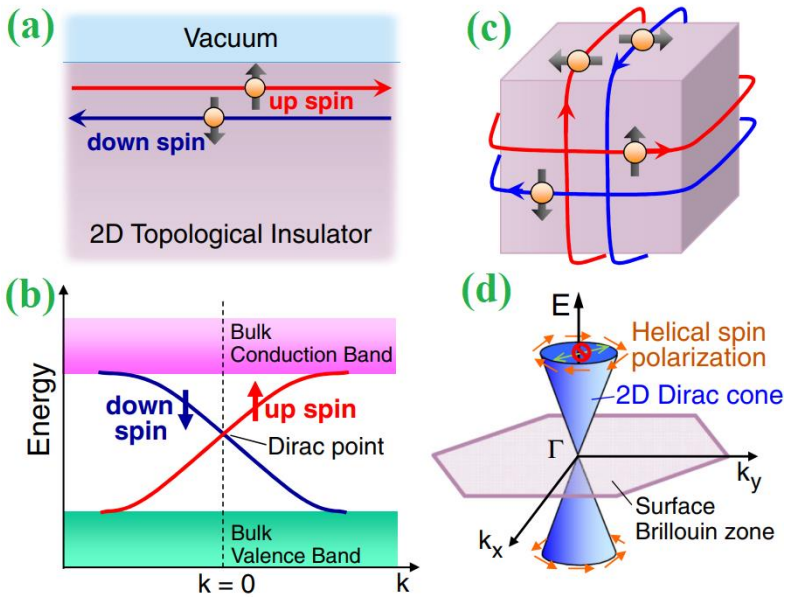

Figure 42: Edge and surface states of topological insulators with Dirac dispersions. **(a)** Schematic real-space picture of the 1D helical edge state of a 2D TI. **(b)** Energy dispersion of the spin non-degenerate edge state of a 2D TI forming a 1D Dirac cone. **(c)** Schematic real-space picture of the 2D helical surface state of a 3D TI. **(d)** Energy dispersion of the spin non-degenerate surface state of a 3D TI forming a 2D Dirac cone [22].

On the other hand, it is known that two-dimensional (2D) confined electrons show a completely different, topological, type of order behavior if they experience strong magnetic fields, leading to quantum Hall effect. The topological order also occurs in some 3D materials, explained by SOC mechanism without applying a magnetic field [20]. Therefore, ideally it is expected that in TIs, electrons could form a quantum Hall state driven by forces that result from their motion through the crystal lattice, instead of being driven by magnetic field [20]. However, in reality SOC does not have the symmetry required to induce the quantum Hall effect, it only leads to mixing of spin-up and spin-down electrons and thus a no conserved spin current is expected [20]. Therefore, a prerequisite to have a 3D strong topological insulator is that all components of the spin mix, driven by SOC [20]. The topological properties of metallic states formed at the surface of a topological insulator are indeed the inheritance from the bulk insulator. The

metallic surface states owe their robustness against disorder or impurities to topological properties of the bulk insulator [20]. Therefore, it is of great importance to have a smooth surface with well-defined momentum along the surface, indicative of the bulk-surface connection [20]. Each momentum along the surface has only a single spin state at the Fermi level, and the spin direction rotates as the momentum moves around the Fermi surface [20].

Consequently, finding a 3D-TI material driven by strong enough SOC with the capability of modifying the electronic structure gives a clear hint to the heavy-element, small-bandgap semiconductors as the appropriate candidates. Since firstly, SOC as a relativistic effect is strong in heavy elements; and secondly, SOC only can change the phase if its energy is much larger than the bandgap energy [20].

Undoubtedly, angle-resolved-photoemission spectroscopy (ARPES) is an effective technique to probe the existence of the topologically protected surface states. At the beginning in order to detect these surface states, a viable alternative to ARPES is offered by transport measurements, but in practice it turns out demanding due to the contribution of both bulk and surface states to conduction. The transport properties of TIs are decided by two crucial factors: the surface spin structure and the Berry phase associated with the surface electrons [23]. Both factors bring about the suppression of backscattering and further delocalization of surface electrons [23].

2.2 Berry Phase

Once a quantum system transports adiabatically around a closed contour C, it acquires a non-integrable phase (Berry phase) depending on the geometry of contour C, besides the dynamical phase. This Berry phase is known as an important parameter for topological phases [18]. The helical spin texture of topological surface states is defined by an in-plane spin of a surface electron locked perpendicularly to its momentum [19]. An adiabatic moving of surface electron around the Fermi circle of surface states leads to the rotation of its spin by 2π, and thus the surface electron acquires a π Berry phase [19, 24].

Due to the wave properties of electrons, to observe the transport phenomena based on the electron interference, it is necessary that the coherence of electrons is preserved [21]. The phase coherence is broken with inelastic scattering processes like phonon scattering (due to lattice vibrations), which is abundant at room temperature [21]. Therefore, it is important to make transport measurements at temperatures of a few Kelvin or even lower [21].

2.2.1 Quantum Diffusion

The electronic transport in solids can be classified by several characteristic lengths [24]:

1. The mean free path (ℓ), which measures the average distance that an electron travels before its momentum is changed by elastic scattering from static scattering centers;
2. The phase coherence length (l_φ), which measures the average distance an electron can maintain its phase coherence. l_φ is usually determined by inelastic scattering from electron-phonon coupling and interaction with other electrons;
3. The sample size (L).

Two transport regimes are considered for electrons [24]:

- The **ballistic transport** regime where $\ell \gg L$ and electrons can tunnel through the sample without being scattered;
- The **diffusive transport** regime where $\ell \ll L$ and electrons experience scattering and diffuse through the sample. In this regime, if $l_\varphi \leq \ell$, semiclassical diffusion occurs and the Drude conductivity governs; else if $l_\varphi \gg \ell$, the **quantum diffusive** regime occurs where the phase coherence of electrons is maintained [24].

In most cases, the electron transport is in diffusive regime. The interference effects in disordered diffusive samples are explained with some closed loops resulting from elastic scatering within the sample. These loops differ in size and geometrical shape due to the statistical distribution of scattering centers. The propagation of electron partial waves within these loops occurs in clockwise and anti-clockwise directions, see **Figure**

43 [21]. The quantum interference between time-reversed scattering loops will give rise to a correction to the conductivity, leading to weak-localization (WL) or weak-antilocalization (WAL) in the quantum diffusive regime [24]. Moreover, transport measurements on materials with 2D gapless Dirac cone like carbon nanotubes and graphene revealed that at low temperatures these systems are in the quantum diffusion regime where the WAL or WL are supposed to occur [24]. Similarly, the surface states of a 3D TI are considered as 2D gapless Dirac fermions [24]. The observation of WAL or WL is reported by several groups in TI films [18, 19, 21, 25-35].

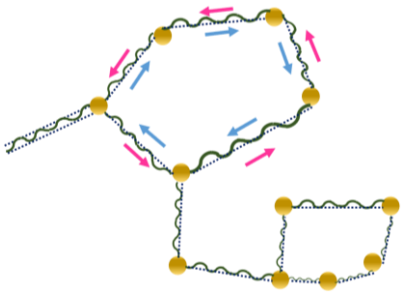

Figure 43: Electron interference in closed loops [21].

The constructive interference at zero magnetic field, independent of the size and shape of loops, leads to the increased overall resistance in comparison with a classical case, known as WL which is a spin-conserving phenomenon [21]. If the spin orientation undergoes a change while the electron moves through the sample due to SOC, then the resultant interference is not necessarily constructive [21]. The total spin rotation of the electrons after the propagation in a closed loop is a function of each particular loop geometry as well as spin-orbit scattering at impurities [21]. Thus, by considering both the spin orientation and the electron phase, the total interference amplitude is destructive on average, leading to an enhanced conductance at zero magnetic field known as WAL phenomenon [21]. These time-reversed scattering loops are equivalent to moving an electron on the Fermi surface by one cycle. As a result, the electron picks up a Berry phase $\varphi_b \equiv (1 - \frac{\Delta}{2E_F})$, where E_F is the Fermi energy and Δ is the bandgap [24]. Therefore, the WAL signature of 2D Dirac Fermions is explained with the Berry phase. In the massless limit, the Berry phase takes π value, leading to a destructive quantum

interference (WAL), while in the large-mass limit, it becomes zero and the quantum interference is constructive (WL) [24].

2.3 Weak localization and weak anti-localization in TIs

An adiabatic moving of an electron around the Fermi surface results in a π Berry phase, in a 3D-TI with helical surface states. Thus, the absence of backscattering, and further delocalization of surface electrons are expected. The experimental signature of electron delocalization in TIs is realized by a WAL effect, due to the destructive quantum interference between time-reversed loops formed by scattering trajectories [24]. Therefore, due to the suppression of decoherence mechanisms at very low temperatures, an increase in conductivity is expected [24].

In terms of definition, the main difference of TIs with ordinary metals is that the TIs benefit from the topologically protected surface states that cannot be localized [24]. However, empirically in most experiments by lowering the temperature, a logarithmic suppression of conductivity was observed. This unexpected behavior occurs in ordinary disordered metals as a precursor of Anderson localization [34, 35], known as a transport paradox in TIs [24]. It is said that in 2D metals complete localization occurs if the electrons are scattered only by normal impurities, therefore they don't exhibit a truly metallic behavior and their conductivity at absolute zero temperature disappears [36]. At higher temperatures, there is a logarithmic temperature dependency of conductivity, a weakly localized regime [36], explained by a small correction to the metallic conductivity by the precursor of complete localization at $T = 0$ [36].

The quantum interference in the weakly localized regime depends on the strength of the spin-orbit scattering and applied magnetic field. The former defines the sign of the correction which is either positive or negative [36, 37], whereas the latter results in the appearance of magnetoresistance (MR) [36, 37]. On the other hand, the interplay between the spin-orbit scattering and Zeeman splitting due to an applied field should be considered, as the Zeeman splitting can break the symmetry of the time-reversed paths if the spin states are not identical everywhere [36, 37]. This means that in the non-interacting electron regime, the Zeeman energy mixes the singlet and triplet states of spin

and thus suppresses the WAL, whereas in the electron-electron interaction regime, the opposite happens and the strong spin-orbit scattering suppresses the Zeeman-split term [36-38]. Therefore, both spin-orbit scattering and Zeeman effect contribute to the appearance of MR. In the weak spin-orbit scattering, MR remains to be negative regardless of the applied field, whereas the strong spin-orbit scattering results in positive MR in weak fields, and it changes sign at higher fields [36], while at finite spin-orbit scattering, the Zeeman splitting yields an always positive MR [37]. The orientation of the magnetic field helps to differentiate between these two mechanisms given the fact that the Zeeman effect exclusively depends on the magnetic-field strength, while the other is flux driven [36, 37].

Quantitatively, for the strong SOC limit, the correction to the magnetoconductivity against the magnetic field is explained with Hikami-Larkin-Nagaoka (HLN) model [39]. In deriving HLN equation, the effect of random magnetic impurity scattering, spin-orbit scattering, magnetic field and inelastic collisions on the quantum backscattering interference term [39] are considered, while the Zeeman energy is not. The HLN equation, giving the change of the conductivity σ with the Field B is

$$\Delta\sigma(B) \approx \alpha \frac{e^2}{2\pi^2\hbar}\left[\psi\left(\frac{1}{2}+\frac{B_\varphi}{B}\right) - \ln\left(\frac{B_\varphi}{B}\right)\right] \tag{2.1}$$

where $B_\varphi = \frac{\hbar}{4el_\varphi^2}$, e is the electronic charge, $\hbar$ is the reduced Planks constant, l_φ is the phase coherence length, and $\psi(x)$ is the digamma function. α can take the values of $1, 0$ and -0.5 for orthogonal, unitary and symplectic cases, respectively [39-41]. Quantum spin texture systems, such as the 2D surface states of a 3D TI, belong to the symplectic class and thus α should be equal to -0.5 for one topological surface and -1 in a film with one top and one bottom surface [40].

In many experiments, the observed crossover from WAL to WL is explained by gap opening mainly by two approaches [24]:

1. **Magnetically doped surface states**: the time-reversal symmetry of gapless surface states of TI is broken by doping magnetic impurities

2. **The finite-size effect of the surface states:** In a thin film of TI, two gapless Dirac cones at the top and bottom surfaces can hybridize to open a finite-size gap, transforming the gapless Dirac cones into two massive Dirac cones. In a given thin film, the crossover is a function of $\frac{\Delta}{E_F}$, where finite-size gap is fixed and E_F can be tuned by the gate voltage [24].

Moreover, in most samples of TIs, the Fermi energy usually crosses not only the surface states, but also the bulk states, and thus WL is expected [24]. The WAL-WL crossover is realized by tuning the Fermi level by gate voltage. Indeed, when the Fermi level is shifted from the bulk gap to the valence or conduction bands, there exist a competition between the bulk electrons and surface electrons [24]. Therefore, in this case it is possible to observe WL [24].

Moreover, the strong spin-orbit scattering in TIs also manifest itself in the logarithmic temperature dependency of longitudinal conductivity on applying low magnetic field [34, 35], arising from the quantum correction to the conductivity of π Berry phase at zero magnetic field [38, 42]

$$\delta\sigma_L(T) = -\alpha\frac{e^2}{\pi h}\ln\left(\frac{\tau_\varphi}{\tau}\right) = \alpha p\frac{e^2}{\pi h}\ln\left(\frac{T}{T_L}\right) \tag{2.2}$$

where τ is the elastic scattering time and T_L is a characteristic temperature at which the quantum correction vanishes. The phase coherence time τ_φ typically varies with the temperature T as $\tau_\varphi \propto T^{-p}$ (The exponent p depends on the source of the inelastic scattering which causes the phase decoherence, e. g., $p = 3$ for phonon scattering, and $p = \frac{2}{3}$ (3D) or $p = 1$ (2D) for the electron-electron interaction [42, 43]; where α is a constant depending on the relative strengths of the spin-orbit and spin-flip (magnetic) scattering. In the limit of weak spin-orbit and magnetic scattering, one obtains $\alpha = 1$; in the limit of strong spin-orbit and weak magnetic scattering, one finds $\alpha = -0.5$; and when the magnetic scattering is strong, $\alpha = 0$ [42]). However, due to the observation of transport paradox in TIs at low temperatures indicating an insulating ground state, the other likely scenario, namely the electron-electron interactions (EEI) is also imagined for

the surface state effects [35]. The correction to the conductivity due to the temperature dependence of the EEI effect for the TI surface states is explained by the conventional EEI effect suggested by P. A. Lee and T. V. Ramakrishnan [35].

$$\delta\sigma_I(T) = -\frac{e^2}{\pi h}(1 - \frac{3}{4}F)\ln(\frac{T}{T_I}) \tag{2.3}$$

where F is the screening factor (a function of the average of the static screen Coulomb interaction over the Fermi surface [42] and T_I is the characteristic temperature for the EEI effect [35]. It is evident that both mechanism explained by equation (2.2) and equation (2.3) are similar in nature, and thus the $\sigma_{xx} - lnT$ plot can be fitted with $\sigma_{xx}(T) = \left(\frac{e^2}{\pi h}\right).\kappa.ln(\frac{T}{T_0})$ to extract κ and F.

2.4 $Pb_{0.77}Sn_{0.23}Se$ Characterization

In order to investigate the topological properties in a TI material experimentally, this study is centered on the Raman and magneto-transport of $Pb_{0.77}Sn_{0.23}Se$. In general, lead-tin-selenide ($Pb_{1-x}Sn_xSe$) alloys in the range of $0 < x < 0.4$ are semiconductors with rocksalt structure [44, 49]. Crystallizing in the rocksalt structure gives high dielectric constants and quite unusual infrared and electronic properties to these alloys [45, 46]. These alloys have a direct electronic bandgap ($E_{gap} \leq 0.29\,eV$), which is located at four equivalent L (111) points on the edge of the Brillouine zone [47, 48]. The energy gap E_{gap} of these alloys strongly depends on both alloy fraction (x) and temperature [49]. $Pb_{0.77}Sn_{0.23}Se$ is considered as a narrow bandgap semiconductor, composed of heavy elements, therefore it is expected that its topological properties rely on SOC mechanism.

Dziawa et al. [50] ARPES studies on $Pb_{0.77}Sn_{0.23}Se$ revealed that it belongs to topological crystalline insulators (TCIs) by observation of Dirac-like surface states formation crossing the bandgap. ARPES is a powerful technique for directly probing the electronic structure of solids, particularly well suited for studying surface states owing to its surface sensitivity [50]. TCIs are a class of TIs with mirror (crystalline) symmetry, instead of time-reversal symmetry present in TIs [18, 19, 50-53]. The mirror symmetry in

TCIs can be easily broken in comparison with time-reversal symmetry [18, 19, 50-53], implying that the topological boundary states can acquire a bandgap under weak perturbations that break the mirror symmetry [52, 53].

Figure 44*:* The bulky cone of $Pb_{0.77}Sn_{0.23}Se$.

The $Pb_{0.77}Sn_{0.23}Se$ single crystals used in this study were grown by means of a modified Bridgeman method where crystal boules of $Pb_{0.77}Sn_{0.23}Se$ were produced following the procedure described by Tanaka et al. [51]. Initially, $Pb-Sn-Se$ boules were synthesized from stoichiometric quantities of high-purity Pb and Sn shots (Alpha Aesar 99.99%) and powders of Sn and Se (Alpha Aesar 99.999%) [54].

Figure 44 depicts the bulky cone of $Pb_{0.77}Sn_{0.23}Se$ produced at University of Warwick. In order to realize the topological properties of this alloy, it was essential to have a device that can allow controlling its topological nature. To meet this goal, aiming at achieving thin films of this alloy, the bulky cone was cleaved using the scalpel along the edge of (001). Thereafter, the tiny cleaved pieces, were exfoliated using the blue scotch tape by conventional mechanical exfoliation technique and transferred to thermally oxidized $Silicon$ substrate covered with $290-nm-thick$ $Silicon\ dioxide$ (SiO_2) layer shortly afterwards. The thickness of the resultant flakes were measured by atomic force microscopy (AFM) technique, see **Figure 45**.

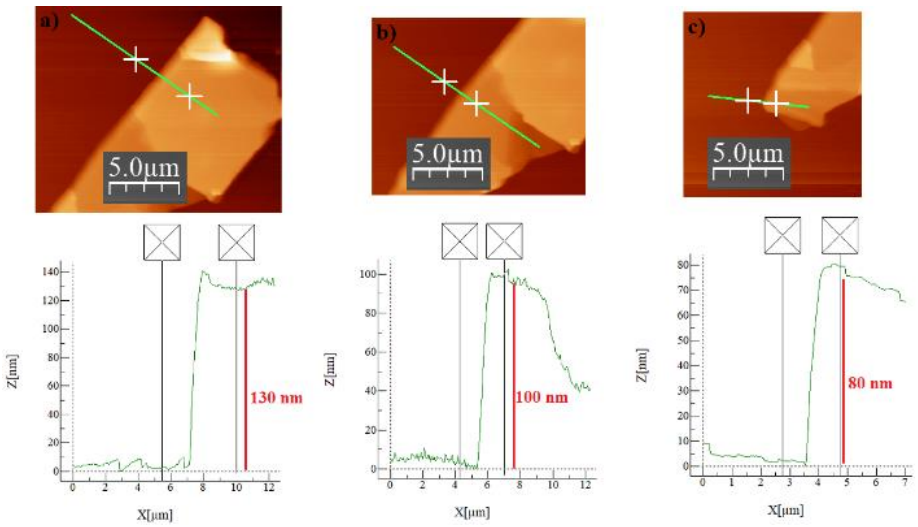

Figure 45: AFM images of exfoliated thin films of $Pb_{0.77}Sn_{0.23}Se$.

Once we took Raman measurements on the resultant flakes, we recognized that the Raman response of the resultant thin films is different than its bulk. The reproducibility of the results were verified by repeating the exfoliation process as well as Raman characterization many times. Thereafter, to explore the topological features of this material, temperature-dependent as well as magnetic-dependent Raman spectroscopy were performed on the exfoliated thin films of $Pb_{0.77}Sn_{0.23}Se$. Moreover, to corroborate the Raman results, some magneto-transport measurements were performed on Hall bar devices of $Pb_{0.77}Sn_{0.23}Se$ thin films, see **Figure 46**.

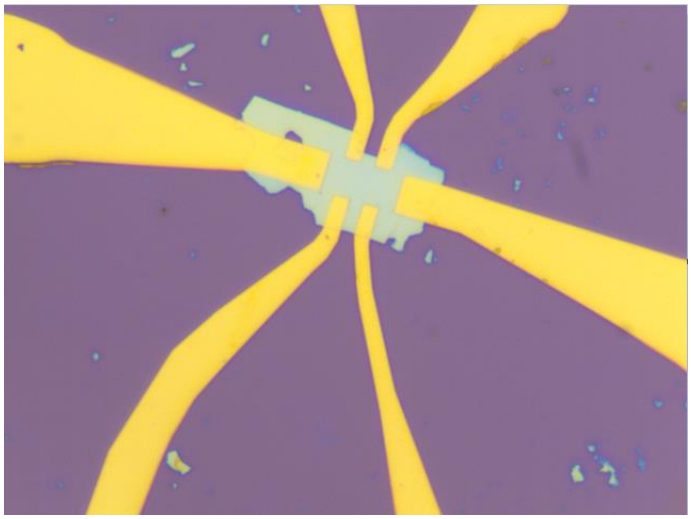

Figure 46: A Hall bar device on $Pb_{0.77}Sn_{0.23}Se$ thin film.

2.5 Raman Response of $Pb_{0.77}Sn_{0.23}Se$

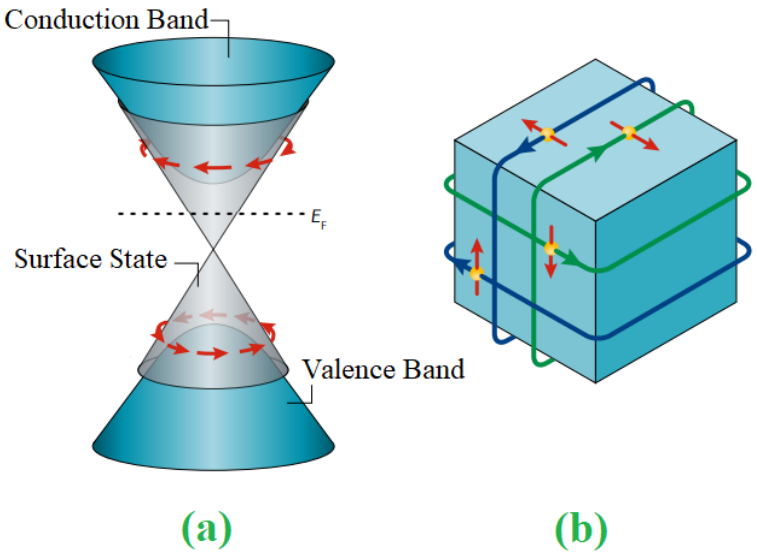

Figure 47: The electronic structure of a TI. (a) The massless Dirac-like dispersion of the surface state with spin-momentum locking in a TI. The surface state band connects the bulk valence and the bulk conduction bands. (b) Real-space picture of the surface state in a TI [55].

It is known that in 3D-TIs, surface states with a linear dispersion exist within the bandgap, and cross each other at the so-called Dirac point. Due to the linear dispersion, the electrons behave like massless relativistic particles; see **Figure 47** [55]. Unlike the 2D TI phases, the experimental discovery of 3D TI phases revealed that there is a possibility to realize a 3D TI phase at room temperature without applying external magnetic field [19]. Moreover, their metallic surface states exist at bare surfaces rather than only at buried interfaces [19]. Consequently, these relaxed conditions (room temperature, no magnetic field and bare surfaces) pave the way for exploring electrical transport and optical properties of topological surface states [19]. Moreover, a distinctive feature of a TI surface comparing with its famous counterpart with Dirac electronic structure (graphene surface) is that the surface Fermi level of a TI does not necessarily sit at the Dirac point [20], and thus there is a competition between surface electrons and bulk electrons for contribution to optical and transport properties [24].

Initially, aiming at finding the contribution of both surface and bulk states, we performed some Raman characterization on thin films, and freshly cleaved bulky samples of $Pb_{0.77}Sn_{0.23}Se$ at relaxed conditions, shortly after sample preparation, see **Figure 48**.

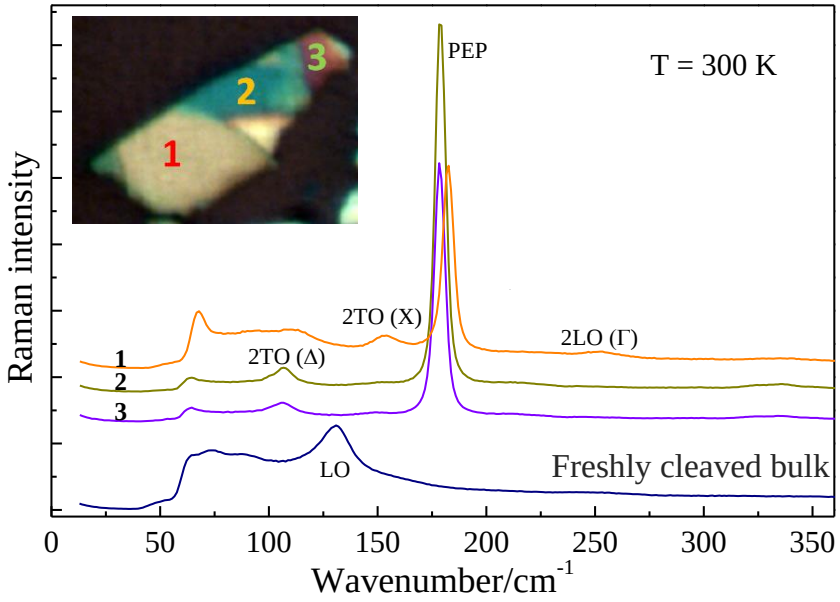

Figure 48: The Raman response of thin films and freshly cleaved bulk samples of $\boldsymbol{Pb_{0.77}Sn_{0.23}Se}$. The thicknesses of areas with labels 1, 2 and 3 are $\boldsymbol{130\ nm}$, $\boldsymbol{100\ nm}$, $\boldsymbol{80\ nm}$, respectively. The spectra have been vertically shifted for clarity.

As depicted in **Figure 48**, for $Pb_{0.77}Sn_{0.23}Se$ thin films, the modes at 111 cm^{-1}, 154 cm^{-1}, 184 cm^{-1} and 250 cm^{-1} are observed. The peak at 130 cm^{-1} observed for the bulky sample is the longitudinal optical (LO) mode, which is absent in the Raman spectra of $Pb_{0.77}Sn_{0.23}Se$ thin films. Indeed, for the thin films, the appearance of this mode is shifted to higher energies, associated with the thickness reduction and thus the more contribution of surface states with respect to bulk states. Therefore, this trend can be explained with strong interaction of the LO phonon modes with electrons. In this regard, the plasma modes of electrons take the significant role, and thus the electron-phonon interaction is described in terms of coupled plasmon-phonon modes [**56**, **57**]. Such optical phonons occupy a limited and well-defined range of wave-vectors close to the center of the Brillouine zone [**58**]. Moreover, the plasmon-phonon coupling strengthens the electron-phonon interaction when the free carrier density in Dirac surface

states increases [59]. For this reason, we call it "**Plasma-enhanced-phonon (PEP)**" peak.

2.5.1 Temperature-dependent Raman measurement of $Pb_{0.77}Sn_{0.23}Se$

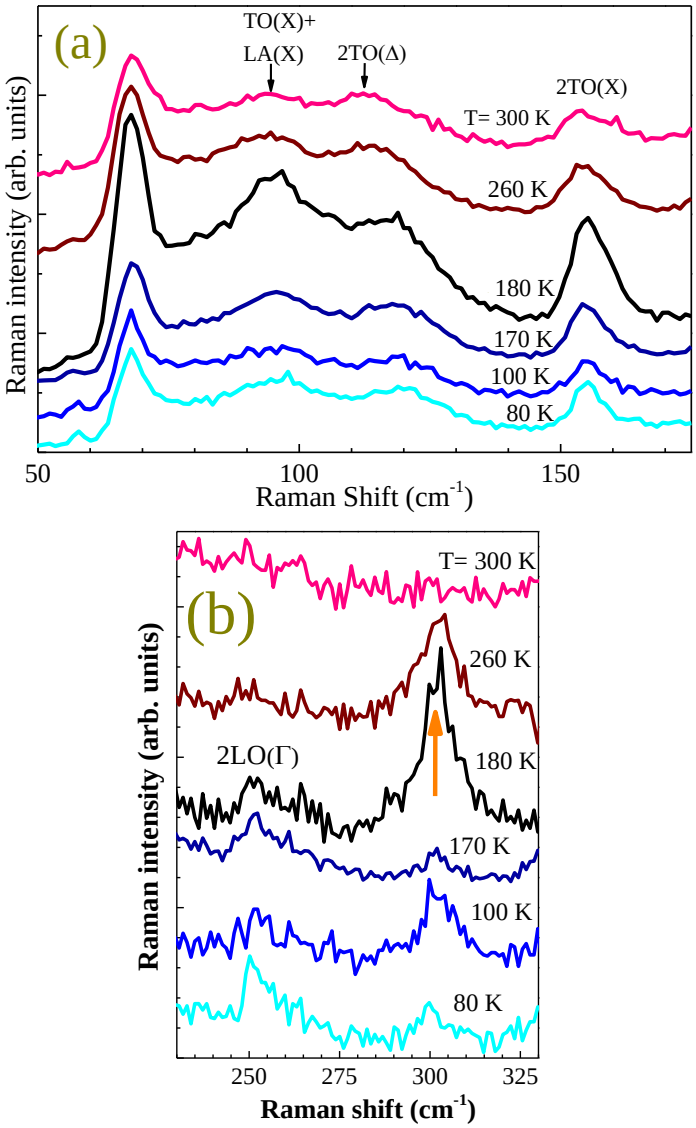

Figure 49: The Raman spectra as a function of temperature measured on an area 1, of **Figure 48 (a)** below and **(b)** above 200 cm^{-1}. The spectra have been vertically shifted, and arrows added (determining the position of some of the peaks) for clarity.

Since ARPES studies on the (001) surface of $Pb_{0.77}Sn_{0.23}Se$ monocrystals revealed that the topological nature and the surface state electronic structure in this

material are sensitive to temperature [60]; we performed some temperature-dependent Raman measurements on $Pb_{0.77}Sn_{0.23}Se$ thin films with the thickness of $130\,nm$, see **Figure 49**. The appearance of a mode close to $300\,cm^{-1}$ (marked with an arrow in **Figure 49** (b)) at the temperature of $180\,K$ is explained with the long-range coupling between the topologically protected surface electrons and phonons which activates the forbidden single LO phonon near the center of the Brillouine zone [58]. Therefore, we attribute this mode to the first overtone of the LO phonon ($2\,LO$), explained by Fröhlich interaction, where the excess energy of carriers is mainly removed by the interaction of LO phonons with the carriers [58]. Another signature of the Fröhlich interaction is that with increasing temperature, its contribution to the $2\,LO$ scattering decreases due to the erosion of the resonance [58].

2.5.2 Anharmonic Decay of optical phonons in $Pb_{0.77}Sn_{0.23}Se$

The thermal properties of solid materials depend on the availability of carriers and the scattering rates. The crucial roles of electron scattering and phonon scattering manifest themselves in electronic transport properties and thermal transport (particularly for the case of insulators where heat is carried mainly by phonons), respectively [61]. Electron scattering brings an electronic system, which has been subjected to external perturbations back to equilibrium [61]. Collisions also alter momentum of all the carriers, as the electrons are brought back into equilibrium [61]. Electron-phonon scattering is the dominant scattering mechanism in metals and crysyalline semiconductors (though with different scattering processes) except at very low temperatures where the phonon density is low [61]. The probability that an electron makes a transition from an initial state i to a final state f is proportional to [61]:

1. the availability of final states for electrons;
2. the probability of absorbing or emitting a phonon;
3. the strength of the electron-phonon coupling/ interaction.

The probability of absorbing or emitting a phonon is proportional to the electron-phonon coupling and to the phonon density $n\,(q)$ for absorption, and the phonon density $(1+$

$n\ (q)$) for emission, where $n\ (q)$ is given by the Bose-Einstein factor $n(q) = \frac{1}{\exp\left(\frac{\hbar\omega(q)}{K_B T}\right)-1}$ [61].

On the other hand, the dominant phonon scattering process in crystalline materials is usually phonon-phonon scattering. Phonons are scattered by other phonons because of anharmonic terms in the restoring potential. This scattering process permits [61]:

1. two phonons to combine to form a third phonon, or
2. one phonon to break up into two phonons

In these anharmonic processes, energy and wavevector conservation apply. The phonon density is proportional to the Bose factor so that the scattering rate is proportional to: $\frac{1}{\tau_{ph}} \sim \frac{1}{\exp\left(\frac{\hbar\omega}{K_B T}\right)-1}$ [61].

Therefore, to discriminate between the surface and bulk contributions to the conduction, characterized by Raman spectroscopy technique, the concepts of anharmonic phonon-phonon interaction as the dominant mechanism present in the bulk and electron-phonon interaction in the surface conduction are taken into account [62]. Electron-phonon interaction manifests itself in strong phonon renormalization depending on temperature [62].

Moreover, in the broad context of optics and transport, the significance of the non-equilibrium optical phonons created by the excited carriers and the resultant thermal issues is easily appreciated [56-58, 63]. Indeed, the tendency of highly excited electrons in the conduction band (created either optically or by applying electric field) is to decay towards their ground state leads to the emission of optical phonons. These optical phonons decay into lower energy phonons through anharmonic coupling. The rate of anharmonic coupling and thus the phonon lifetime are critical parameters in modeling of high-field transport, e. g. an unwelcome hot phonon effect (due to the small anharmonic rate of the optical phonons) on the optical and electronic transport properties of the electronic devices [56-58, 63].

To investigate the phonon dynamics of the $2\,LO$ mode in Raman spectra of $Pb_{0.77}Sn_{0.23}Se$, we have extracted the values of frequency ω and the linewidth Γ (Full

Width at Half Maximum (FWHM)) by fitting the temperature-dependent Raman data with the Voigt profile [62]. This is a probability distribution obtained from a convolution of Lorentz distribution and a Gaussian distribution, given by

$$y = y_0 + (f_1 * f_2)(x) \tag{2.4}$$

with

$$f_1(x) = \frac{2A}{\pi}\frac{\omega_L}{(x - x_c)^2 + (\omega_L)^2} \tag{2.5}$$

and

$$f_2(x) = \sqrt{\frac{4\ln(2)}{\pi}}\frac{\exp(-\frac{4\ln(2)}{\omega_G^2}.x^2)}{\omega_G} \tag{2.6}$$

Therefore, we can write

$$y = y_0 + A\frac{2\ln(2)}{\pi^{3/2}}\frac{\omega_L}{\omega_G^2}\int_{-\infty}^{\infty}\frac{\exp(-t^2)}{(\sqrt{\ln(2)}\frac{\omega_L}{\omega_G})^2 + (\sqrt{4\ln(2)}\frac{x - x_c}{\omega_G} - t)^2}dt \tag{2.7}$$

where ω_G (Gaussian line-shape) and ω_L (Lorentzian line-shape) are the linewidth of both convoluted peaks, A is the integrated area of the Lorentzian peak and y_0 is the offset. While the full width at half maximum is given by

$$FWHM = 0.5346 \times \omega_L + \sqrt{(0.2166\omega_L^2 + \omega_G^2)} \tag{2.8}$$

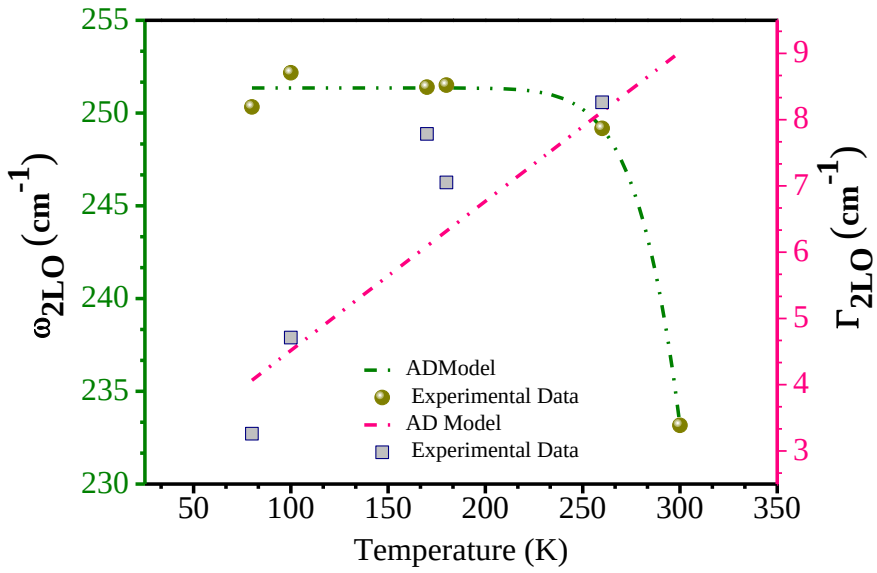

Figure 50: Self-energy effects from Voigt fits of the temperature-dependent Raman response. The dark yellow spheres and blue squares stand for extracted frequencies and linewidths from 2LO mode, respectively. The pink and violet dashed lines are fits using the model of anharmonic decay.

Figure 50 depicts the frequency and linewidth of the temperature-dependent Raman response of 2 LO mode fitted with Voigt profile; ω_{2LO} decreases with increasing temperature, while the linewidth gets broader. These trends give a hint to the contribution of two phonon-induced mechanisms (Fröhlich interaction and anharmonic decay of optical phonons). Generally, the excited carriers tend to decay towards the ground states by emission of optical phonons. Here, the involved optical phonons are the LO ones (with the wavevectors close to the center of the Brillouine zone). Through Fröhlich interaction, the excess energy of carriers is removed and the optical phonons decay into lower energy phonons through anharmonic coupling [58, 62, 64, 65]. To verify this idea, the frequency and linewidth values are fitted with the model of anharmonic decay (AD) (a symmetric decay of the optical phonon into two acoustic phonons with lower energies), given by [62, 63, 65]

$$\begin{aligned}\omega(T) &= \omega_0 + \Delta\omega^{(1)}(T) + \Delta\omega^{(2)}(T) \\ &= \omega_0 + \Delta\omega^{(1)}(T) + A[1 + n(\omega_1) + n(\omega_2)]\end{aligned} \tag{2.9}$$

where ω_0 is the bare harmonic frequency, $\Delta\omega^{(1)}$ is quasi-harmonic correction (due to the thermal expansion of the crystal lattice) and $\Delta\omega^{(2)}$ is the anharmonic phonon-phonon coupling term. The linewidth is given by

$$\Gamma(T) = B(1 + n(\omega_1) + n(\omega_2)) \tag{2.10}$$

where $\omega_1 = \omega_2 = \frac{\omega_0}{2}$ and $n(\omega) = \frac{1}{\exp\left(\frac{\hbar\omega}{K_B T}\right)-1}$; A and B are fitting parameters [62, 65, 66].

As depicted in **Figure 50**, the experimental data are in good agreement with the AD model, indicating that there is a phonon-phonon interaction as the dominant scattering mechanism, typical behavior of semiconductors and insulators. As a result, the contribution of both bulk and surface states in $Pb_{0.77}Sn_{0.23}Se$ thin film with the thickness of $130\,nm$ is verified through anharmonic decay of optical phonons and Fröhlich interaction, respectively.

2.5.3 Magnetic-dependent Raman measurement in $Pb_{0.77}Sn_{0.23}Se$

As depicted in **Figure 49**, the mode $2\,TO\ (X)$ is always present in the Raman spectra of $Pb_{0.77}Sn_{0.23}Se$ with temperature changes. To investigate more about this mode, some other thinner films with $35\,nm$ thickness were prepared as the thickness reduction helps the more contribution of surface states to bulk ones. Thereafter, at room temperature, some magnetic-dependent Raman measurements were performed on prepared samples at weak magnetic fields up to $0.35\,T$. It is known that the characteristic feature of a 3D-TI is the presence of strong SOC, promising the helical surface states with topologically protected unidirectional transport of electrons [21, 67-69]. As depicted in **Figure 51**, the mode $2\,TO\ (\Delta)$ remained unchanged to the applied magnetic field. While the peak $2\,TO\ (X)$ does not shift, but at $0.2\,T$ a big surge in the peak is observed which progressively disappears at fields between $0.2\,T$ and $0.35\,T$, explained with the fact that as long as the protection of the surface states is guaranteed by the symmetry, the peak $2\,TO\ (X)$ is observed. Once the symmetry is broken, the peak disappears. The PEP peak associated with surface states is shifted to higher frequencies against the applied magnetic field with a rate of 3.6 cm^{-1}/T. This blue shift has its origin in the spin of

electrons, since the applied magnetic field is in the weak regime. In the weak magnetic field regime ($\omega_c = \frac{eB}{m^*}$ the cyclotron frequency) the carriers are scattered long before completing a single cyclotron orbit in real space [61]. Therefore, the observed trends rely on SOC instead of an external magnetic field [61]. Moreover, the observation of the PEP peak against the applied magnetic fields gives a hint that under the applied conditions the surface states are continuously connected within the gap and the surface is conductive.

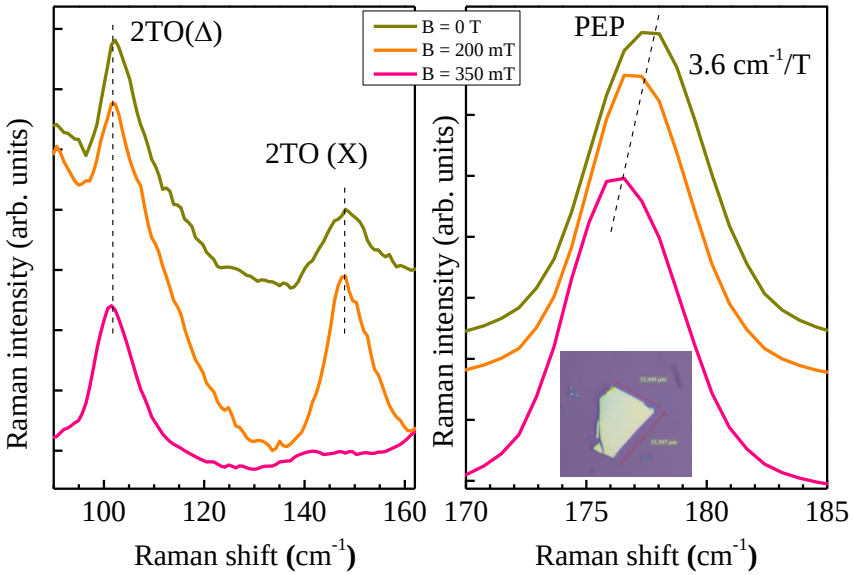

Figure 51: Magnetic-field dependent Raman spectra of $Pb_{0.77}Sn_{0.23}Se$ thin films; the spectra have been vertically shifted for clarity.

2.6 Magnetotransport Measurements of Hall-bar devices of $Pb_{0.77}Sn_{0.23}Se$

Figure 52 depicts the temperature-dependent longitudinal resistance of the device in the absence of a magnetic field. For the temperatures above 100 K, the longitudinal resistance has a semiconducting trend, indicating the Fermi level lying in or near the bulk bandgap. While, for the temperature range of 50-100 K, the curve trend switches to a metallic behavior. As marked in **Figure 52** with a green arrow, at temperature 150 K there is an abrupt change in the resistance against temperature. Dixon and Hoff [70] explained this abrupt change near $150\ K$ as a direct consequence of the discontinuity in the temperature coefficient of the gap energy. According to their studies, the abrupt

changes in the range of $50 - 150\,K$ is due to the thermal excitation of carriers, while above $150\,K$ clear from the curve trend, the carriers are nearly equal and temperature independent. This behavior may give some transport evidence on the ARPES results of Dziawa et al [50] regarding the evolution of the gapped surface states into the Dirac-like state for the temperatures below $100\,K$. As the temperature drops below $50\,K$, there is a drastic increase in the longitudinal resistance, indicating the insulating ground state, resulting from a strong electron-electron interaction. Plotting the longitudinal resistance against temperature in a longitudinal scale and the linear behavior of the curve (like in 2D disordered metals) implies that there is a strong localization; in agreement with Zhang et al [33] studies on $Pb_{1-x}Sn_xSe$ thin films with $10\,nm$ thickness (for different tin concentrations $x = 0.07,\ x = 0.25,\ x = 0.32,\ x = 0.43$). The resistance of their most insulating sample ($x = 0.25$) reached at $10^8\Omega$ at low temperatures [33].

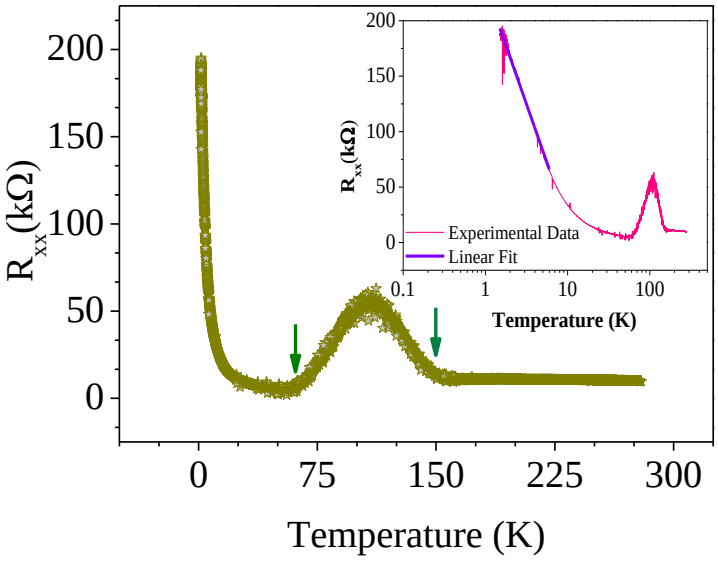

Figure 52: Temperature-dependent resistance of a thin film of $Pb_{0.77}Sn_{0.23}Se$ with $35\,nm$ thickness. The linear trend of the resistance against the temperature at low temperatures in a logarithmic scale (a sign of strong localization) is plotted in the inset. The violet solid line is a linear fit.

Since it is known that the manifestation of both Berry phase and EEI effect occur with the dependency of conductivity on $ln\,(T)$, we have performed some temperature-dependent measurements to record the magnetoresistance at low magnetic fields, see fig. The σ_{xx} versus lnT curve is fitted with $\sigma_{xx}(T) = \left(\frac{e^2}{\pi h}\right).\kappa.\ln(\frac{T}{T_0})$, See **Figure 53**. The

extracted κ and T_0 parameters are plotted against the applied magnetic field. The difference in κ between the absence and presence of magnetic field is attributed to the Berry phase effect, as it is the dominant mechanism at zero and low magnetic fields. For $B > 0.2\ T$, κ is almost constant and independent of the magnetic field, explained by the strong SOC. To verify the role of this effect, we obtain $\alpha P = 0.2$. For the dephasing by two- and three-dimensional electron-electron scattering, $P = 1$ and $P = \frac{2}{3}$ are expected, respectively [43]. Moreover, for the EEI effect, we have $(1 - \frac{3}{4}F) = 0.22$ and the extracted F value is 1.04. Thus, the presence of insulating ground state is explained with EEI effect due to scattering between the bulk and surface states. The extracted values give a hint that a contribution from the surface states is not that big to provide the WAL effect. In this case, most probably, the Fermi energy crosses not only the surface states, but also the bulk states, and thus WL is expected.

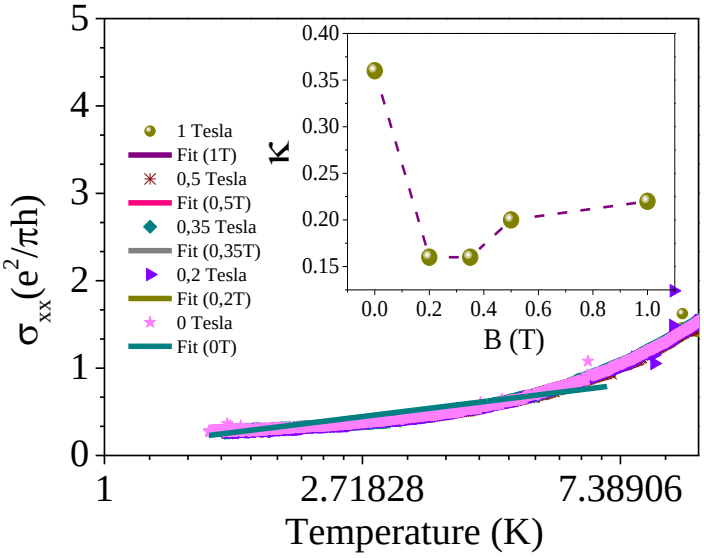

Figure 53: The temperature dependency of σ_{xx} recorded at B=0, 0.2, 0.35, 0.5 and 1T. The solid lines are the linear best fits in the logarithmic scale. In the inset, the slope (κ) of the $\sigma_{xx}(B) - lnT$ plot against the applied magnetic field is plotted.

To shift the Fermi level from the valence or conduction band to the bulk gap and investigate the presence of WAL effect and tuneability of the Berry phase, we have performed magnetotransport measurements on our samples as well as applying an external gate bias to tune the Fermi level at 1.5 K (See **Figure 54** and **Figure 55**). The

obtained data were fitted with HLN equation $(\sigma(B)-\sigma(0)=\frac{\alpha}{\pi}[\psi\left(\frac{1}{2}+\frac{\hbar}{4eBl_{\varphi}^{2}}\right)-\ln(\frac{\hbar}{4eBl_{\varphi}^{2}})])$ [39] to extract the prefactor α as well as the phase coherence length l_{φ}, see **Table III**.

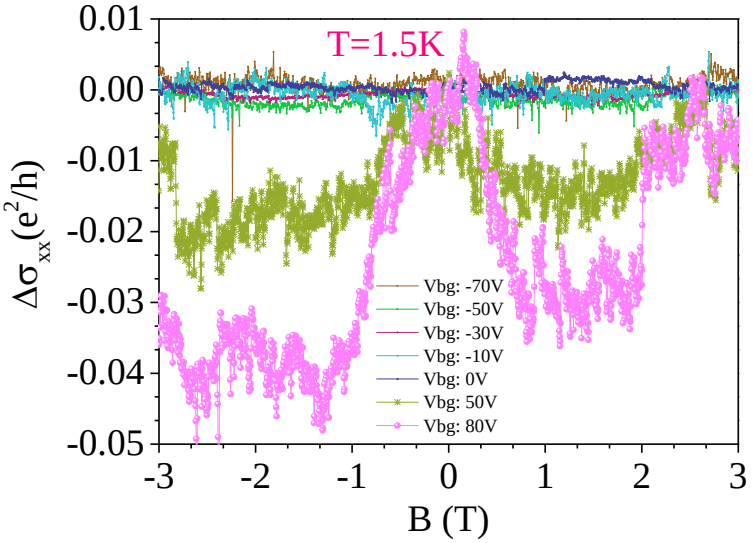

Figure 54: Tuning the magnetoconductivity from WL to WAL by applying the external gate bias from (-70 V) to (80 V).

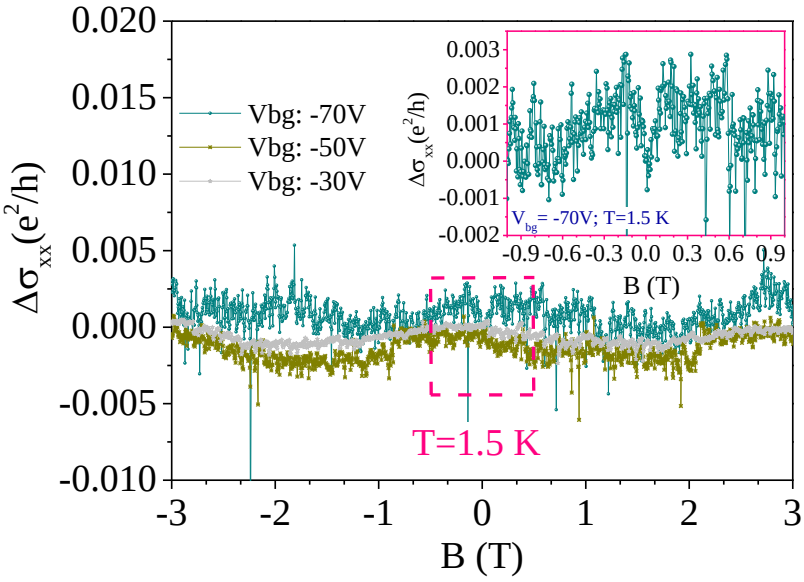

Figure 55: The appearance of WL signature by approaching the high negative voltages by applying (-70V) external gate bias.

Table III: Fitting parameters α and l_φ, obtained by fitting HLN equation for a thin film of $Pb_{1-x}Sn_xSe$ ($x = 0.23$) with 35 nm thickness.

V_{bg} (V)	α	l_φ (m)
0, -10, -30, -50, -70 (WL)	-	-
50 (WAL)	- 0.0044	7.75×10^{-9}
80 (WAL)	- 0.046	1.61×10^{-9}

The results are consistent with Zhang et al. [33] studies on $Pb_{1-x}Sn_xSe$ thin films with 10 nm thickness (for different tin concentrations $x = 0.07$, $x = 0.25$, $x = 0.32$, $x = 0.43$). The obtained value of α is far away from the expected theoretical value ($\alpha = -0.5$) for one topological surface state. This deviation arises from the SOC driven contribution of both bulk and surface states to the coherent transport. The observed WAL-WL crossover as a function of the applied backgate voltage $(80\ V) - (-70\ V)$, may be explained by gap opening due to finite-size effect of surface states. In a thin film of TIs, the hybridization of gapless Dirac cones on the top and bottom surfaces leads to a finite size gap. As for a given thin film, the finite-size gap (Δ) is fixed, thus the crossover depends on $\frac{\Delta}{E_F}$, where E_F can be tuned by the gate voltage. Moreover, the theoretical studies of Ozawa et al [71] on another TCI ($Pb_{1-x}Sn_xSe$ thin films), revealed that TCI films due to their stronger finite size effect compared to their 3D TI peers stand as a potential candidate for bipolar transport applications, since the Fermi level can be tuned to the Dirac point on the surface states of the bulk TCI by applying a gate voltage [71]. In these materials, the energy gap is largely a function of thin film thickness [71]. Moreover, the paradox exists between the observed strong localization behavior at low temperatures and the WAL signature around the zero magnetic field (See **Figure 54**). It is suggested to solve this dilemma by considering the fact that the theories of the conventional electrons fail for the case of TIs, since the topological properties of TIs are explained with massless Dirac fermions as the topological surface electrons as well as the bulk electrons [72]. In this regard, H-Z. Lu and S-Q. Shen studies [72] help to interpret this paradox by considering simultaneously the role of both electron-electron interactions to explain the unexpected temperature dependency as well as the role of quantum interference correction in case of magnetoresistance.

As we have already shown that the role of EEI effects is pronounced in our results, to differentiate between the SOC and Zeeman effect as the probable origins of the observed negative magnetoconductance [**36**, **37**], we have performed some other measurements with a tilted magnetic field. As depicted in **Figure 56**, the rotation of magnetic field orientation towards 0° weakens the negative magnetoconductance, suggesting that the role of Zeeman effect is negligible, and the observed WAL signature is due to the strong SOC.

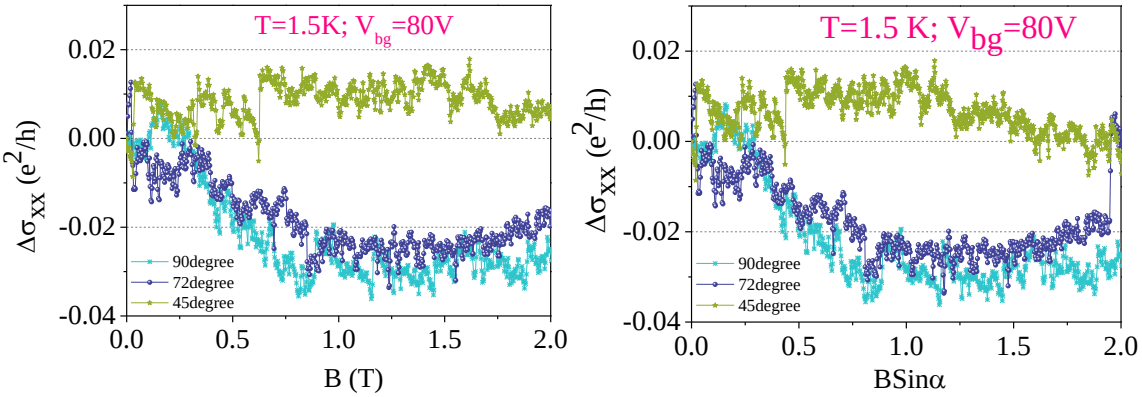

Figure 56: Left: Variation of magnetoconductivity at 1.5 K and applied backgate voltage of 80 V with respect to the magnetic field at different orientations; **Right:** Variation of magnetoconductivity as a function of the perpendicular field component at 1.5 K and backgate voltage of 80 V.

2. 7 Conclusion & Outlook

In this chapter, with the help of Raman and magneto-transport characterizations, the topological properties of $Pb_{0.77}Sn_{0.23}Se$ are investigated and the presence of surface states as well as their symmetry-protection are confirmed. Moreover, the observation of WL-WAL crossover gives a hint to the tuneability of the Berry phase, explained by a surface gap opening due to the strong finite size effect.

Chapter 3

This thesis is aimed at studying the topological properties of a 3D-TCI, $Pb_{0.77}Sn_{0.23}Se$. For this reason, initially, we have tried to learn about the fundamental topological properties of TIs and TCIs in order to be able to plan some strategies to realize these properties experimentally. Based on our theoretical literature reviews, a 3D-TI phase at room temperature can be realized without applying a magnetic field. Therefore, at the very first step, Raman characterization was performed on exfoliated flakes of this material at relaxed conditions and the presence of surface states as a result of plasmon-phonon interactions was confirmed by appearance of the PEP peak. In the second step, by changing a temperature parameter and making temperature-dependent Raman characterization, the contribution of both surface states and bulk counterparts were explained by two phonon-induced mechanisms Fröhlich interaction and anharmonic decay of optical phonons, respectively. The presence of the peak TO (X) at all applied temperature ranges made us to find the origin of the physical interpretation behind this peak. For this reason, we performed some low-magnetic field Raman characterization on thinner flakes and thus higher contribution of surface states. Our results indicate that the surface states are topologically protected as long as the symmetry is not broken, while the surface states remain conductive under all circumstances. The observation of these topological signatures gives a hint to the strong spin-orbit coupling present in this material. To corroborate this idea, we have performed some magneto-transport measurements on Hall-bar devices of this material. Our results demonstrated that there is a strong electron-electron interaction in this material. By applying an external gate bias within the range of $-70\,V$ to $80\,V$, the WL-WAL crossover is observed, explained by tuneability of the Berry phase. Moreover, the observed WAL effect had spin-orbit coupling origin, while the negligibility of the Zeeman effect is clarified by applying the tilted magnetic field.

Our findings paved the way for the electron studies in field-effect transistors (FET) functioning, based on the topological phase transition [18]. An ultrahigh speed operation due to the high carrier mobility and dissipationless operation due to the absence of the backscattering is expected for topological transistors [18]. To meet this objective,

one or two high-κ dielectric gate layer and a substrate along with the topological channel are required [**18**]. The phase conversion (switching behavior) between a TCI to normal insulator is realized by tuning an electric field. Moreover, since the carrier transport occurs at the surfaces of the topological layer via topological surface states, a high quality interface at the heterostructure of the topological transistor is required [**18**].

Publication List and Conference contributions:

1. Summer school on "**Cryogenics, microwave measurements and low temperature engineering for quantum technology,**" Cryocourse 2018, Low Temperature Laboratory, Aalto University, Finland, September 21-26, 2018.

2. Flatlands beyond Graphene 2019, Toulouse, France, September 2-6, 2019. Poster Section: "The Raman Spectroscopic Characterization and Transport Measurements on Exfoliated Flakes of $Pb_{0.77}Sn_{0.23}Se$ topological crystalline insulator".

3. S. Mehdipour, D. López-Diaz, M. M. Velázquez, P. Hidalgo, B. Méndez, M. Luna, V. Bellani, M. Amado, G. Balakrishnan, and E. Diez, *Journal of Raman Spectroscopy*, vol. *51*, pp.2489-2495, 2020.

4. Workshop and Summer School on **"Basics and Applications of Nanolithography,"** Salamanca, Spain, 29-30 June & 1 July, 2021,. Poster Section: "Magneto Phonon Resonance and Anharmonic Decay of Optical Phonons in $Pb_{0.77}Sn_{0.23}Se$ Nanoflakes".

5. Invited talk, Conmat 2021, Valencia, Spain 18-20 October, 2021, "Low Magnetic Field and temperature-dependent Raman response and tuneable Berry Phase in thin films of $Pb_{0.77}Sn_{0.23}Se$."

6. S. Mehdipour, A. Perez-Rodriguez, V. Bellani, P. Hidalgo, B. Mendez, G. Balakrishnan, M. Amado and E. Diez, "Tuneable Berry Phase and Electron Correlation in $Pb_{0.77}Sn_{0.23}Se$ Topological Crystalline Insulator Thin Films" (To be submitted).

References:

[1] W. Whyte, Cleanroom design, John Wiley & sons Ltd, 1999.

[2] J. F. O'Hanlon, A user's guide to vacuum technology. John Wiley & Sons, 2005.

[3] A. Sarangan, Nanofabrication: Principles to Laboratory Practice. CRC Press, 2016.

[4] Fundamentals of vacuum technology, www.oerlikon.com

[5] A. Fridman. Plasma chemistry. Cambridge university press, 2008.

[6] C. Mack. Fundamental principles of optical lithography: the science of microfabrication. John Wiley & Sons, 2008.

[7] M. O. Lamminen, H. W. Walker, and L. K. Weavers. "Mechanisms and factors influencing the ultrasonic cleaning of particle-fouled ceramic membranes," Journal of membrane science 237, 213-223, 2004.

[8] W. Kim, T. H. Kim, J. Choi, & H. Y. Kim, “Mechanism of particle removal by megasonic waves,” Applied Physics Letters, 94. 081908, 2009.

[9] Y. Min, and Z. Shen. "A review on mechanical exfoliation for the scalable production of graphene," Journal of Materials Chemistry A 3, 11700-11715, 2015.

[10] Y. Huang, et al. "Reliable exfoliation of large-area high-quality flakes of graphene and other two-dimensional materials," ACS nano 9, 10612-10620, 2015.

[11] Scanning Electron Microscope A to Z, www.jeol.com

[12] P. Vandenabeele, Practical Raman Spectroscopy: an introduction, John Wiley & Sons, 2013.

[13] J. R. Ferraro, K. Nakamoto and C. W. Brown, “Introductory Raman Spectroscopy,” Elsevier, 2003.

[14] Z. Zhao and C. Wang, Cryogenic Engineering and Technologies, CRC Press, Taylor & Fransis Group, 2020.

[15] TeslatronPT Manual, Oxford Instruments Nanoscience. https://www.oxinst.com/

[16] M. A. Tupta, AC versus DC measurement methods for low-power nanotech and other sensitive devices, Keithly. https://www.tek.com/keithley

[17] J. M. Maxson, Using a Lock-in amplifier, Lehigh university department of Physics 262, 2008.

[18] M. M. H. Polash, Sh. Yalameha, H. Zhou, K. Ahadi, Z. Nourbakhsh, D. Vashaee, Materials Science and Engineering Reports vol. 145, 100620, 2021.

[19] F. Ortmann, S.Roche, S. O. Valenzuela, Topological Insulators: Fundamentals and Perspectives, John Wiley & Sons, 2015.

[20] J. E. Moore, Nature vol. 464, 194, 2010.

[21] T. Schäpers, Semiconductor Spintronics, Walter de Gruyer GmbH, 2016.

[22] Y. Ando, Journal of the Physical Society of Japan, vol. 82, 102001, 2013.

[23] J. Chen, X. Y. He, K. H. Wu, Z. Q. Ji, L. Lu, J. R. Shi, J. H. Smet, Y. Q. Li, Physical Review B, Vol. 83, 241304, 2011.

[24] H-Z. Lu, S-Q. Shen, Spintronics VII, Proceedings of SPIE vol. 9167, 2014.

[25] J. Chen, X. Y. He, K. H. Wu, Z. Q. Ji, L. Lu, J. R. Shi, J. H. Smet, Y. Q. Li, Physical Review B **83**, 241304, 2011.

[26] H-Z. Lu, S-Q. Shen, Spintronics VII, Proceedings of SPIE Volume 9167, 2014.

[27] A. Roy, S. Guchhait, S. Sonde, R. Dey, T. Pramanik, A. Rai, H. C. P. Movva, L. Colombo, S. K. Banerjee, Applied Physics Letter **102**, 163118, 2013.

[28] Y. Takagaki, B. Jenichen, U. Jahn, M. Ramsteiner, K.-J. Friedland, Physical Review B **85**, 115314, 2012.

[29] S-P. Chiu, J-J. Lin, Physical Review B **87**, 035122, 2013.

[30] M. Liu, C-Z. Chang, Z. Zhang, Y. Zhang, W. Ruan, K. He, L-l. Wang, X. Chen, J-F. Jia, S-C. Zhang, Q-K. Xue, X. Ma, Y. Wang, Physical Review B **83**, 165440, 2011.

[31] H-T. He, G. Wang, T. Zhang, I-K. Sou, G. K. L. Wong, J-N. Wang, Physical Review Letters, **106**, 166805, 2011.

[32] Z. Wang, L. Yang, X. Zhao, Z. Zhang, X. P. A. Gao, Nano Research **8**, 9, 2963, 2015.

[33] C. Zhang, Y. Liu, X. Yuan, W. Wang, S. Liang, F. Xiu, Nano letters **15**, 2161, 2015.

[34] G. Bergmann, Physics Reports vol. 107, 1, 1984.

[35] P. A. Lee, T. V. Ramakrishnan, Reviews of modern Physics vol. 57, 287, 1985.

[36] S. Maekawa, H. Fukuyama, Journal of the physical society of Japan vol. 50, 8, 2516, 1981.

[37] D. Kowal, M. Ben-Chorin, Z. Ovadyahu, Physical Review B vol. 44, 9080, 1991.

[38] G. Tkachov, E. M. Hankiewicz, Physical Review B vol. 84, 035444, 2011.

[39] S. Hikami, A. I. Larkin, Y. Nagaoka, Prog. Theor. Phys vol. 63, 2707, 1980.

[40] H-T. He, G. Wang, T. Zhang, I-K. Sou, G. K. L. Wong, J-N. Wang, Physical Review Letters vol. 106, 166805, 2011.

[41] F. J. Dyson, Journal of Mathematical Physics vol. 3, 140, 1962.

[42] Y. Takagaki, B. Jenichen, U. Jahn, M. Ramsteiner, K.-J. Friedland, Physical Review B, vol. 85, no. 11, p. 115314, 2012.

[43] J. Wang, A. M. DaSilva, C-Z. Chang, K. He, J. K. Jain, N. Samarth, X-C. Ma, Q-K. Xue, M. H. W. Chan, Physical Review B vol. 83, p. 245438, 2011.

[44] A. J. Strauss, Physical review vol. 157, no. 3, p. 608, 1967.

[45] O. Madelung, Semiconductors: Data handbook, Springer, Berlin, pp. 566-605, 2004.

[46] N. Anand, S. Buvaev, A. F. Hebard, D. B. Tanner, Z. Chen, Z. Li, K. Choudhary, S. B. Sinnott, G. Gu and C. Martin, Physical Review B vol. 90, pp. 235143(10), 2014.

[47] G. Nimtz and B. Schlicht, in Narrow Gap Semiconductors (G. Hohler et al.) (Springer Tracts in Modern Physics, vol. 98, Springer, 1983).

[48] D. R. Khokhlov et al., in Lead Chalcogenides: Physics and Applications (Taylor and Francis, 2003).

[49] J. R. Dixon and G. F. Hoff, Physical Review B vol. 3, p. 4299, 1971.

[50] P. Dziawa, B. J. Kowalski, K. Dybko, R. Buczko, A. Szczerbakow, M.Szot, E. Lusakowska, T. Balasubramanian, B. M. Wojek, M. H. Berntsen, O. Tjernberg, T. Story, Nature Materials vol. 11, 1023, 2012.

[51] Y. Tanaka, Z. Ren, T. Sato, K. Nakayama, S. Souma, T. Takahashi, K. Segawa, and Y. Ando, Nature Physics, vol. 8, pp.800-803, 2012.

[52] J. Liu, T. H. Hsieh, P. Wei, W. Duan, J. Moodera, L. Fu, Nature materials vol. 13, 178, 2014.

[53] T. H. Hsieh, H. Lin, J. Liu, W. Duan, A. Bansil, L. Fu, Nature Communications vol. 3, 1, 2012.

[54] G. Balakrishnan, M. Saghir, M. R. Lees, S. J. York, S. A. Hindmarsh, A. M. Sanchez, M. Walker, and C. F. McConville, Journal of the Indian Institute of Science, vol. 96, pp.121-130, 2016.

[55] Y. Tokura, K. Yasuda and A. Tsukazaki, Nature Reviews Physics, vol. 1, pp. 126-143, 2019.

[56] B. K. Ridley, Quantum Processes in Semiconductors, OUP Oxford, (1999).

[57] A. Dyson, B. K. Ridley, Journal of Applied Physics **103**, 114507 (2008).

[58] S. Barman, G. P. Srivastava, Physical Review B **69**, 235208 (2004).

[59] Yuri D. Glinka, S. Babakiray, and D. Lederman, Journal of Applied Physics **118**, 135713, 2015.

[60] A. A. Reijnders, J. Hamilton, V. Britto, J.-B Brubach, P. Roy, Q. D. Gibson, R.J. Cava, and K. S. Burch, Physical Review B 90, 235144, 2014.

[61] M. Dresselhaus, G. Dresselhaus, S. B. Cronin, A. G. Souza Filho, Springer-Verlag GmbH, 2018.

[62] S. Buchenau, S. Scheitz, A. Sethi, J. E. Slimak, T. E. Glier, P. K. Das, T. Dankwort, L. Akinsinde, L. Kienle, A. Rusydi, C. Ulrich, S. L. Cooper, M. Rubhausen, Physical Review B **101**, 245431, 2020.

[63] I. Chatzakis, H. Yan, D. Song, S. Berciaud, T. F. Heinz, Physical Review B **83**, 205411, 2011.

[64] G. D. Smith, S. Firth, R. J. H. Clark, M. Cardona, Journal of Applied Physics **92**, 4375, 2002.

[65] Y. Kim, X. Chen, Z. Wang, J. Shi, I. Miotkowski, Y. P. Chen, P. A. Sharma, A. L. Lima Sharma, M. A. Hekmaty, Z. Jiang, D. Smirnov, Applied Physics Letters **100**, 071907, 2012.

[66] B. Irfan, S. Sahoo, A. P. S. Gaur, M. Ahmadi, M. J.-F. Guinel, R. S. Katiyar, R. Chatterjee, Journal of Applied Physics **115**, 173506, 2014.

[67] S. Guddala, F. Komissarenko, S. Kiriushechkina, A. Vakulenko, M. Li, V. M. Menon, A. Alù, and A. B. Khanikaev, Science 374, 225, 2021.

[68] S. Barik, A. Karasahin, C. Flower, T. Cai, H. Miyake, W. DeGottardi, M. Hafezi, and E. Waks, Science 359, 666, 2018.

[69] N. Parappurath, F. Alpeggiani, L. Kuipers, and E. Verhagen, Science Advances 6, eaaw 4137, 2020.

[70] J. H. Dixon, G. F. Hoff, Physical Review B **3**, 4299, 1971.

[71] H. Ozawa, A. Yamakage, M. Sato, Y. Tanaka, Physical Review B **90**, 045309, 2014.

[72] H-Z. Lu and S-Q. Shen, Physical Review Letters **112**, 146601, 2014.